The Astrophysical Journal, 710:133–149, 2010 February 10 doi:10.1088/0004-637X/710/1/133

FERMI OBSERVATIONS OF CASSIOPEIA AND CEPHEUS: DIFFUSE GAMMA-RAY EMISSION IN THE OUTER GALAXY

A. A. Abdo[1,2], M. Ackermann[3], M. Ajello[3], L. Baldini[4], J. Ballet[5], G. Barbiellini[6,7], D. Bastieri[8,9], B. M. Baughman[10], K. Bechtol[3], R. Bellazzini[4], B. Berenji[3], E. D. Bloom[3], E. Bonamente[11,12], A. W. Borgland[3], J. Bregeon[4], A. Brez[4], M. Brigida[13,14], P. Bruel[15], T. H. Burnett[16], S. Buson[9], G. A. Caliandro[17], R. A. Cameron[3], P. A. Caraveo[18], J. M. Casandjian[5], C. Cecchi[11,12], Ö. Çelik[19,20,21], A. Chekhtman[1,22], C. C. Cheung[1,2], J. Chiang[3], S. Ciprini[12], R. Claus[3], J. Cohen-Tanugi[23], L. R. Cominsky[24], J. Conrad[25,26,52], C. D. Dermer[1], F. de Palma[13,14], S. W. Digel[3], E. do Couto e Silva[3], P. S. Drell[3], R. Dubois[3], D. Dumora[27,28], C. Farnier[23], C. Favuzzi[13,14], S. J. Fegan[15], W. B. Focke[3], P. Fortin[15], M. Frailis[29], Y. Fukazawa[30], S. Funk[3], P. Fusco[13,14], F. Gargano[14], N. Gehrels[19,31,32], S. Germani[11,12], G. Giavitto[6,7], B. Giebels[15], N. Giglietto[13,14], F. Giordano[13,14], T. Glanzman[3], G. Godfrey[3], I. A. Grenier[5], M.-H. Grondin[27,28], J. E. Grove[1], L. Guillemot[27,28,33], S. Guiriec[34], A. K. Harding[19], M. Hayashida[3], D. Horan[15], R. E. Hughes[10], M. S. Jackson[26,35], G. Jóhannesson[3], A. S. Johnson[3], W. N. Johnson[1], T. Kamae[3], H. Katagiri[30], J. Kataoka[36], N. Kawai[37,38], M. Kerr[16], J. Knödlseder[39], M. Kuss[4], J. Lande[3], L. Latronico[4], M. Lemoine-Goumard[27,28], F. Longo[6,7], F. Loparco[13,14], B. Lott[27,28], M. N. Lovellette[1], P. Lubrano[11,12], A. Makeev[1,22], M. N. Mazziotta[14], J. E. McEnery[19,32], C. Meurer[25,26], P. F. Michelson[3], W. Mitthumsiri[3], T. Mizuno[30], C. Monte[13,14], M. E. Monzani[3], A. Morselli[40], I. V. Moskalenko[3], S. Murgia[3], P. L. Nolan[3], J. P. Norris[41], E. Nuss[23], T. Ohsugi[30], A. Okumura[42], N. Omodei[4], E. Orlando[43], J. F. Ormes[41], D. Paneque[3], V. Pelassa[23], M. Pepe[11,12], M. Pesce-Rollins[4], F. Piron[23], T. A. Porter[44], S. Rainò[13,14], R. Rando[8,9], M. Razzano[4], A. Reimer[3,45], O. Reimer[3,45], T. Reposeur[27,28], A. Y. Rodriguez[17], F. Ryde[26,35], H. F.-W. Sadrozinski[44], D. Sanchez[15], A. Sander[10], P. M. Saz Parkinson[44], C. Sgrò[4], E. J. Siskind[46], P. D. Smith[10], G. Spandre[4], P. Spinelli[13,14], J.-L. Starck[5], M. S. Strickman[1], A. W. Strong[43], D. J. Suson[47], H. Takahashi[30], T. Tanaka[3], J. B. Thayer[3], J. G. Thayer[3], D. J. Thompson[19], L. Tibaldo[5,8,9], D. F. Torres[17,48], G. Tosti[11,12], A. Tramacere[3,49], Y. Uchiyama[3], T. L. Usher[3], V. Vasileiou[20,21], N. Vilchez[39], V. Vitale[40,50], A. P. Waite[3], P. Wang[3], B. L. Winer[10], K. S. Wood[1], T. Ylinen[26,35,51], and M. Ziegler[44]

[1] Space Science Division, Naval Research Laboratory, Washington, DC 20375, USA
[2] National Research Council Research Associate, National Academy of Sciences, Washington, DC 20001, USA
[3] W. W. Hansen Experimental Physics Laboratory, Kavli Institute for Particle Astrophysics and Cosmology, Department of Physics and SLAC National Accelerator Laboratory, Stanford University, Stanford, CA 94305, USA
[4] Istituto Nazionale di Fisica Nucleare, Sezione di Pisa, I-56127 Pisa, Italy
[5] Laboratoire AIM, CEA-IRFU/CNRS/Université Paris Diderot, Service d'Astrophysique, CEA Saclay, 91191 Gif sur Yvette, France; isabelle.grenier@cea.fr
[6] Istituto Nazionale di Fisica Nucleare, Sezione di Trieste, I-34127 Trieste, Italy
[7] Dipartimento di Fisica, Università di Trieste, I-34127 Trieste, Italy
[8] Istituto Nazionale di Fisica Nucleare, Sezione di Padova, I-35131 Padova, Italy; luigi.tibaldo@pd.infn.it
[9] Dipartimento di Fisica "G. Galilei," Università di Padova, I-35131 Padova, Italy
[10] Department of Physics, Center for Cosmology and Astro-Particle Physics, The Ohio State University, Columbus, OH 43210, USA
[11] Istituto Nazionale di Fisica Nucleare, Sezione di Perugia, I-06123 Perugia, Italy
[12] Dipartimento di Fisica, Università degli Studi di Perugia, I-06123 Perugia, Italy
[13] Dipartimento di Fisica "M. Merlin" dell'Università e del Politecnico di Bari, I-70126 Bari, Italy
[14] Istituto Nazionale di Fisica Nucleare, Sezione di Bari, 70126 Bari, Italy
[15] Laboratoire Leprince-Ringuet, École polytechnique, CNRS/IN2P3, Palaiseau, France
[16] Department of Physics, University of Washington, Seattle, WA 98195-1560, USA
[17] Institut de Ciencies de l'Espai (IEEC-CSIC), Campus UAB, 08193 Barcelona, Spain
[18] INAF-Istituto di Astrofisica Spaziale e Fisica Cosmica, I-20133 Milano, Italy
[19] NASA Goddard Space Flight Center, Greenbelt, MD 20771, USA
[20] Center for Research and Exploration in Space Science and Technology (CRESST) and NASA Goddard Space Flight Center, Greenbelt, MD 20771, USA
[21] Department of Physics and Center for Space Sciences and Technology, University of Maryland Baltimore County, Baltimore, MD 21250, USA
[22] George Mason University, Fairfax, VA 22030, USA
[23] Laboratoire de Physique Théorique et Astroparticules, Université Montpellier 2, CNRS/IN2P3, Montpellier, France
[24] Department of Physics and Astronomy, Sonoma State University, Rohnert Park, CA 94928-3609, USA
[25] Department of Physics, Stockholm University, AlbaNova, SE-106 91 Stockholm, Sweden
[26] The Oskar Klein Centre for Cosmoparticle Physics, AlbaNova, SE-106 91 Stockholm, Sweden
[27] CNRS/IN2P3, Centre d'Études Nucléaires Bordeaux Gradignan, UMR 5797, Gradignan, 33175, France
[28] Université de Bordeaux, Centre d'Études Nucléaires Bordeaux Gradignan, UMR 5797, Gradignan, 33175, France
[29] Dipartimento di Fisica, Università di Udine and Istituto Nazionale di Fisica Nucleare, Sezione di Trieste, Gruppo Collegato di Udine, I-33100 Udine, Italy
[30] Department of Physical Sciences, Hiroshima University, Higashi-Hiroshima, Hiroshima 739-8526, Japan
[31] Department of Astronomy and Astrophysics, Pennsylvania State University, University Park, PA 16802, USA
[32] Department of Physics and Department of Astronomy, University of Maryland, College Park, MD 20742, USA
[33] Max-Planck-Institut für Radioastronomie, Auf dem Hügel 69, 53121 Bonn, Germany
[34] Center for Space Plasma and Aeronomic Research (CSPAR), University of Alabama in Huntsville, Huntsville, AL 35899, USA
[35] Department of Physics, Royal Institute of Technology (KTH), AlbaNova, SE-106 91 Stockholm, Sweden
[36] Waseda University, 1-104 Totsukamachi, Shinjuku-ku, Tokyo 169-8050, Japan
[37] Department of Physics, Tokyo Institute of Technology, Meguro City, Tokyo 152-8551, Japan
[38] Cosmic Radiation Laboratory, Institute of Physical and Chemical Research (RIKEN), Wako, Saitama 351-0198, Japan
[39] Centre d'Étude Spatiale des Rayonnements, CNRS/UPS, BP 44346, F-30128 Toulouse Cedex 4, France
[40] Istituto Nazionale di Fisica Nucleare, Sezione di Roma "Tor Vergata," I-00133 Roma, Italy
[41] Department of Physics and Astronomy, University of Denver, Denver, CO 80208, USA

[42] Department of Physics, Graduate School of Science, University of Tokyo, 7-3-1 Hongo, Bunkyo-ku, Tokyo 113-0033, Japan
[43] Max-Planck Institut für extraterrestrische Physik, 85748 Garching, Germany
[44] Santa Cruz Institute for Particle Physics, Department of Physics and Department of Astronomy and Astrophysics, University of California at Santa Cruz, Santa Cruz, CA 95064, USA
[45] Institut für Astro-und Teilchenphysik and Institut für Theoretische Physik, Leopold-Franzens-Universität Innsbruck, A-6020 Innsbruck, Austria
[46] NYCB Real-Time Computing Inc., Lattingtown, NY 11560-1025, USA
[47] Department of Chemistry and Physics, Purdue University Calumet, Hammond, IN 46323-2094, USA
[48] Institució Catalana de Recerca i Estudis Avançats (ICREA), Barcelona, Spain
[49] Consorzio Interuniversitario per la Fisica Spaziale (CIFS), I-10133 Torino, Italy
[50] Dipartimento di Fisica, Università di Roma "Tor Vergata," I-00133 Roma, Italy
[51] School of Pure and Applied Natural Sciences, University of Kalmar, SE-391 82 Kalmar, Sweden
Received 2009 October 18; accepted 2009 December 18; published 2010 January 15

ABSTRACT

We present the analysis of the interstellar γ-ray emission measured by the *Fermi* Large Area Telescope toward a region in the second Galactic quadrant at $100^\circ \leqslant l \leqslant 145^\circ$ and $-15^\circ \leqslant b \leqslant +30^\circ$. This region encompasses the prominent Gould Belt clouds of Cassiopeia, Cepheus, and the Polaris flare, as well as atomic and molecular complexes at larger distances, like that associated with NGC 7538 in the Perseus arm. The good kinematic separation in velocity between the local, Perseus, and outer arms, and the presence of massive complexes in each of them, make this region well suited to probe cosmic rays (CRs) and the interstellar medium beyond the solar circle. The γ-ray emissivity spectrum of the gas in the Gould Belt is consistent with expectations based on the locally measured CR spectra. The γ-ray emissivity decreases from the Gould Belt to the Perseus arm, but the measured gradient is flatter than expectations for CR sources peaking in the inner Galaxy as suggested by pulsars. The $X_{\rm CO} = N({\rm H_2})/W_{\rm CO}$ conversion factor is found to increase from $(0.87 \pm 0.05) \times 10^{20}$ cm^{-2} (K km s^{-1})$^{-1}$ in the Gould Belt to $(1.9 \pm 0.2) \times 10^{20}$ cm^{-2} (K km s^{-1})$^{-1}$ in the Perseus arm. We derive masses for the molecular clouds under study. Dark gas, not properly traced by radio and microwave surveys, is detected in the Gould Belt through a correlated excess of dust and γ-ray emission: its mass amounts to $\sim$50% of the CO-traced mass.

Key words: cosmic rays – gamma rays: diffuse background – ISM: clouds

Online-only material: color figures

1. INTRODUCTION

Galactic interstellar γ-ray emission is produced through the interactions of high-energy cosmic rays (CRs) with the gas in the interstellar medium (ISM; via pion production and Bremsstrahlung) and with the interstellar radiation field (via inverse Compton, IC, scattering). Thus, since early studies with the COS-B satellite, diffuse γ rays were recognized to be a tracer of the CR densities and of ISM column densities in the Galaxy (Lebrun et al. 1983; Strong et al. 1988; Bloemen 1989).

The interpretation of the observed emission is often based on two radio tracers of the interstellar gas: the 21 cm line of the hyperfine transition of atomic hydrogen (H I) is used to derive its column density N(H I); the 2.6 mm line of the rotational transition $J = 1 \rightarrow 0$ of CO is used to trace the molecular gas. The molecular phase of the ISM is composed mainly of H_2 which cannot be traced directly in its cold phase. It has long been verified, primarily using virial mass estimates, that the brightness temperature of CO integrated over velocity, $W_{\rm CO}$, roughly scales with the total molecular mass in the emitting region (see, e.g., Solomon & Barret 1991). The conversion factor that transforms $W_{\rm CO}$ into H_2 column density is known as $X_{\rm CO} = N({\rm H_2})/W_{\rm CO}$ (Lebrun et al. 1983).

The $X_{\rm CO}$ conversion factor has often been assumed to be uniform across the Galaxy. We now have evidence, however, that it should increase in the outer Galaxy: from virial masses (Digel et al. 1990), from COBE/DIRBE studies (Sodroski et al. 1995, 1997), and from the measurement of the Galactic metallicity gradient (Israel 1997, 2000). A precise estimate of the $X_{\rm CO}$ gradient is necessary to measure the masses of distant H_2 clouds, but it also impacts the derivation of the distribution of CR sources from γ-ray observations (Strong et al. 2004b).

For many years, supernova remnants (SNRs) have been considered the best candidates as CR sources. We have recently detected possible signatures of hadron acceleration in SNRs thanks to γ-ray observations in the TeV (Albert et al. 2007; Aharonian et al. 2008; Acciari et al. 2009) and GeV domain (Abdo et al. 2009d). However, the origin of Galactic CRs is still mysterious and, on the other hand, the distribution of SNRs in the Galaxy is very poorly determined (Case & Bhattacharya 1998), leading to large uncertainties in the models of diffuse γ-ray emission. The γ-ray emissivity gradient of the diffuse H I gas can provide useful constraints on the CR-density distribution.

Since the Doppler shift of the radio lines allows kinematic separation of different structures along a line of sight, it is possible to constrain the γ-ray emissivities and the subsequent $X_{\rm CO}$ ratios in specific Galactic regions. The performance of the previous γ-ray telescopes did not allow very precise measurements beyond the solar circle (Digel et al. 1996, 2001). The situation has recently been improved with the successful launch of the *Fermi Gamma-ray Space Telescope* on 2008 June 11. The Large Area Telescope (LAT) on board the *Fermi* mission (Atwood et al. 2009) has a sensitivity more than an order of magnitude greater than the previous instrument EGRET on board the *Compton Gamma-ray Observatory* and a superior angular resolution.

We present here the analysis of the interstellar γ radiation measured by the *Fermi* LAT in a selected region of the second Galactic quadrant, at $100^\circ \leqslant l \leqslant 145^\circ$, $-15^\circ \leqslant b \leqslant +30^\circ$, during the first 11 months of the science phase of the mission. The region was chosen because here the velocity gradient with Galactocentric distance is very steep, resulting in good

[52] Royal Swedish Academy of Sciences Research Fellow, funded by a grant from the K. A. Wallenberg Foundation.

kinematic separation which allows four different regions to be defined along each line of sight: the nearby Gould Belt, the main part of the local arm, and the more distant Perseus and outer spiral arms. Among the most conspicuous clouds, one finds Cassiopeia, the Cepheus, and Polaris flares in the Gould Belt (Perrot & Grenier 2003; Heithausen & Thaddeus 1990; Grenier et al. 1989), the most massive molecular complex in the Perseus arm associated with NGC 7538 and Cas A (Ungerechts et al. 2000), and the off-plane molecular cloud in the Perseus arm associated with NGC 281 (Sato et al. 2007). These prominent cloud complexes are well suited to probe CRs and the ISM. The motivations of this work are both to provide improved constraints for diffuse emission models to be used in the detection and analysis of LAT sources and to reach a better comprehension of the physical phenomena related with diffuse γ-ray emission in the outer Galaxy.

2. INTERSTELLAR GAS

Here, we describe the preparation of the maps tracing the column densities of the different components of the ISM, used in the following section to analyze LAT data.

2.1. Radio and Microwave Data

2.1.1. H I

Column densities N(H I) of atomic hydrogen have been derived using the LAB H I survey by Kalberla et al. (2005). The LSR velocity[53] coverage spans from -450 km s^{-1} to +400 km s^{-1} with a resolution of 1.3 km s^{-1}. The survey angular resolution is about 0.°6. Owing to the strong absorption against the radio continuum emission of the Cas A SNR, the H I column densities within 0.°5 from its position were determined by linear interpolation of the adjacent lines.

The column densities have been derived by applying an optical depth correction for a uniform spin temperature T_S = 125 K, in order to directly compare our results with previous studies (like Digel et al. 1996). There is not general agreement in the literature about the values of the spin temperature in the atomic phase of the ISM. From observations of the 21 cm line of H I seen in absorption, Mohan et al. (2004a, 2004b) derived for our region values of T_S varying from ∼50 K to $\gtrsim$ 2000 K, with a mean value ∼125 K. Recently, Dickey et al. (2009), on the basis of other H I absorption surveys, reported a mean value in the second Galactic quadrant T_S = 250 K, almost constant with Galactocentric radius. The maximum difference between the values of N(H I) obtained with T_S = 125 K and those obtained in the optically thin approximation (corresponding to the lower possible amount of gas or to the limit of very high spin temperature) is 30%–40%, whereas the maximum difference between T_S = 250 K and optically thin approximation is 10%–15%. The optical depth correction is nonlinear, so assessing the effects of the approximation is not trivial: in particular we note that the uncertainties are larger where the gas density is higher and that assuming lower values for T_S, we obtain structured excesses in modeled diffuse γ-ray intensities following the shape of the clouds.

The systematic errors are even larger in the Galactic plane where self absorption phenomena become important, especially in the Perseus arm where the subsequent uncertainties of derived N(H I) can reach 30% (Gibson et al. 2005).

[53] Local standard of rest velocity, i.e., the velocity in a reference frame following the motion of the solar system.

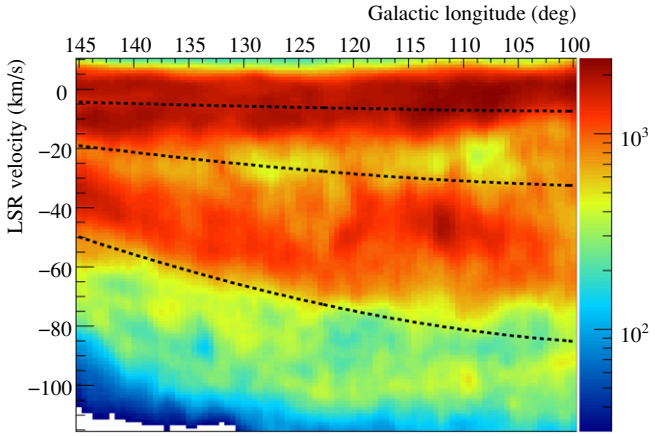

Figure 1. H I longitude–velocity diagram obtained by integrating the brightness temperature in Kalberla et al. (2005) for $|b| < 10°$. The color scale is logarithmic in units of deg K. The three curves bound the preliminary Galactocentric rings used for analysis. At R = 8.8 kpc, R = 10 kpc, and R = 14 kpc (from top to bottom) they roughly separate the Gould Belt, local arm, Perseus, and outer arm. The separation between the Gould Belt and main part of the local arm is hard to distinguish in this diagram.

(A color version of this figure is available in the online journal.)

2.1.2. CO

Intensities W_{CO} of the 2.6 mm line of CO have been derived from the composite survey of Dame et al. (2001), with sampling every 0.°125 near the Galactic plane and in the Gould Belt clouds, supplemented with observations at 0.°25 sampling for high-latitude clouds (>5°), covering in particular the region of NGC 281.

Lines of sight not surveyed in CO were restored by linear interpolation of adjacent directions where possible; otherwise they were assumed to be free of significant CO emission. CO data have been filtered with the moment-masking technique in order to reduce the noise while keeping the resolution of the original data and retaining the edges of the CO clouds (see, e.g., Dame et al. 2001, Section 2.3). Preserving the faint CO edges is important to help decrease the degree of spatial correlation that naturally exists between the N(H I) and W_{CO} maps of a given cloud complex because of the ISM multi-phase structure.

2.2. Kinematic Separation of the Galactic Structures

Our aim is to separately determine the γ-ray emission from the different Galactic structures present along the line of sight in the second quadrant:

1. the very nearby complexes in the Gould Belt, within ∼300 pc from the solar system;
2. the main part of the local arm, typically ∼1 kpc away;
3. the Perseus arm, 2.5–4 kpc away;
4. the outer arm and beyond.

The separation between the Gould Belt and local-arm components is important to probe for a possible change in CR densities between the quiescent nearby clouds of Cassiopeia and Cepheus that produce few low-mass stars, and the more active regions of the local arm which shelter several OB associations (Grenier et al. 1989).

The good kinematic separation of the interstellar gas in this part of the sky is illustrated in Figure 1. The separation of the structures along the line of sight was achieved through a three-step procedure:

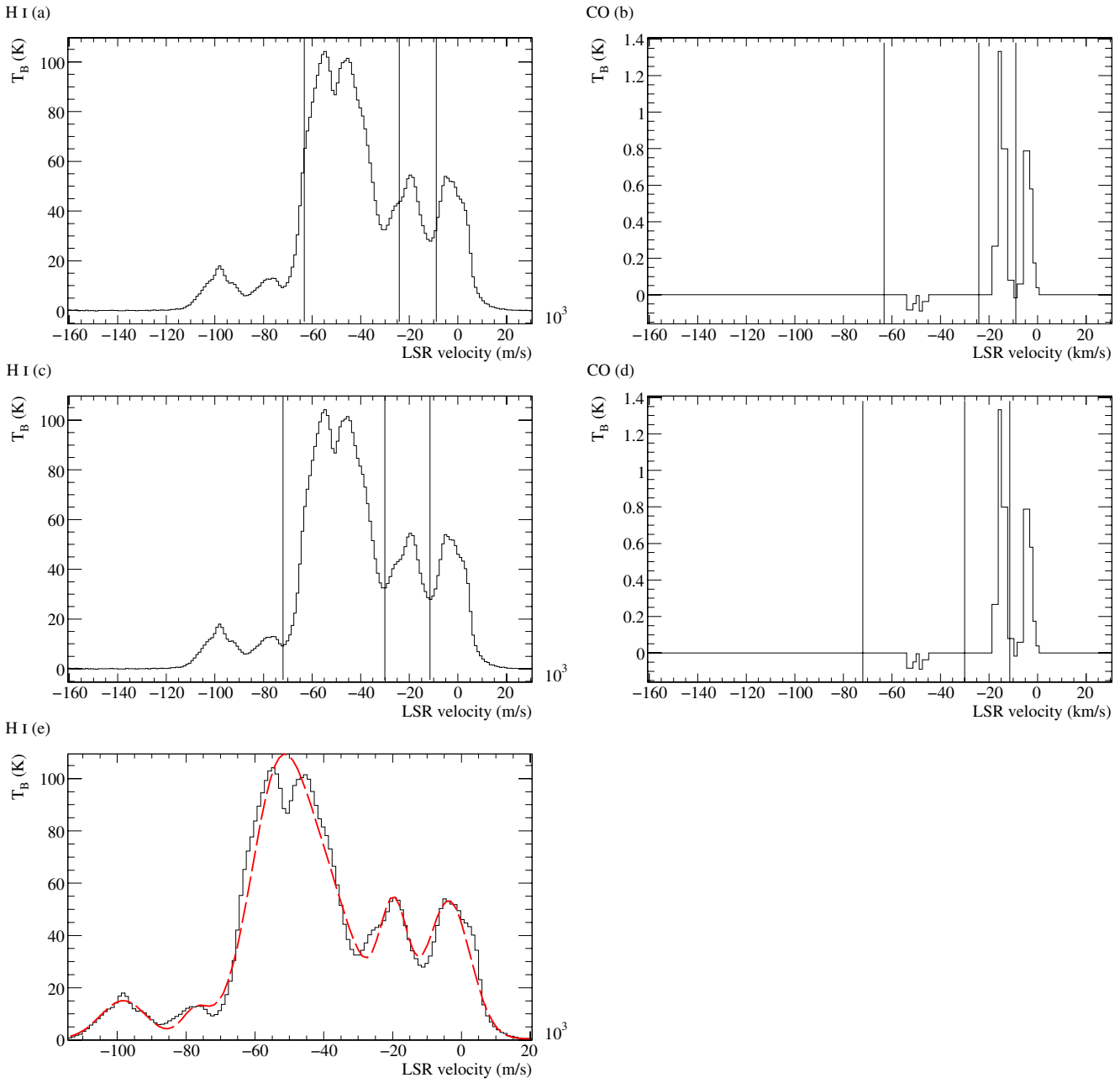

Figure 2. Example of the separation procedure described in Section 2.2 for the direction $l = 133°$, $b = 0°$. Each plot shows the brightness temperature T_B for H I or CO as a function of LSR velocity. Vertical lines correspond to the boundaries Gould Belt–local arm, local arm–Perseus arm, Perseus arm–outer arm (from right to left). The three rows correspond to (1) preliminary ring boundaries (panels (a) & (b)), (2) "physical" boundaries (panels (c) & (d)), and (3) Gaussian fitting of the H I line (panel (e)).

(A color version of this figure is available in the online journal.)

1. preliminary separation based on Galactocentric rings;
2. transformation of the ring-velocity boundaries into "physical" boundaries based on the (l, b, v) coherence of clouds, and production of $N(\mathrm{H\,I})$ and W_{CO} maps;
3. correction of the $N(\mathrm{H\,I})$ maps for the spill-over between adjacent regions.

The three steps are described in detail below. In Figure 2, the procedure is illustrated for an example direction at $l = 133°$, $b = 0°$.

The preparation of the gas maps started from preliminary velocity boundaries given in terms of Galactocentric rings that roughly encompass the Gould Belt for $R < 8.8$ kpc, the main part of the local arm at 8.8 kpc $< R <$ 10 kpc, the Perseus arm at 10 kpc $< R <$ 14 kpc, and the outer arm for $R >$ 14 kpc. Following IAU recommendations, we adopted a flat rotation curve with $R_\odot = 8.5$ kpc and a rotation velocity of 220 km s^{-1} at the solar circle. The confusion that is apparent in the longitude–velocity (l, v) diagram of Figure 1 between the Gould Belt and local-arm components results from the integration over latitude and is much reduced in the actual (l, b, v) cube which is used to construct the maps. The presence of two different components is evident in the example direction of Figure 2: the first component peaks at $v \sim 0$ km s^{-1} (Gould Belt), the second one at $v \sim -15$ km s^{-1} (local arm).

Starting from this preliminary separation, the ring-velocity boundaries were adjusted for each line of sight to better separate structures on the basis of their coherence in the (l, b, v) phase space. For each line of sight, every boundary was moved to the nearest minimum in the H I spectrum, or, if a minimum was not found, to the nearest saddle. The shifts are typically of the order of 1–10 km s^{-1} (see Figures 2(c) and (d)). The adjusted boundaries were used to calculate N(H I) and $W_{\rm CO}$ in each region.

The broad H I clouds can easily spill-over from one velocity interval into the next. To correct for this cross-contamination between adjacent intervals, for each line of sight the H I spectrum has been fitted by a combination of Gaussians (see Figure 2(e)). The overlap estimated from the fit was used to correct the column density N(H I) calculated in a specific interval from the spill-over from the adjacent regions. The correction on N(H I) is typically of the order of 1%–10%, although it can reach 20%–30% in regions corresponding to the frontier between clouds in the Gould Belt and in the main part of the local arm.

This separation scheme provides more accurate estimates of the actual gas mass in a specific region and helps with separating structures. The resulting maps are shown in Figure 3. They exhibit a low level of spatial degeneracy between the cloud complexes found in the four regions along these directions. Hence, we can model the observed γ-ray flux as a combination of contributions coming from CR interactions in the different regions. The correlation between the H I and CO phases in each region is unavoidable, but not tight enough to hamper the separation between the γ-ray emission from the two phases. No significant CO emission is found in the outer-arm region, so the corresponding map was removed from the analysis.

2.3. Interstellar Reddening

An excess of γ rays (observed by EGRET) correlated with an excess of dust thermal emission was found over the N(H I) and $W_{\rm CO}$ column-density maps in all the nearby Gould Belt clouds by Grenier et al. (2005). Therefore, they reported a considerable amount of "dark" gas, i.e., neutral gas not properly traced by H I and CO, at the interface between the two radio-traced phases. The chemical state of the additional gas has not been determined yet, leaving room for H_2 poorly mixed with CO or to H I, overlooked, e.g., because of incorrect assumptions about the spin temperature for optical depth corrections or H I self absorption (see Section 2.1.1).

Following the method proposed by Grenier et al. (2005), we have prepared a map to account for the additional gas. The map is derived from the $E(B-V)$ reddening map of Schlegel et al. (1998), which provides an estimate of the total dust column densities across the sky. Point sources (corresponding to *IRAS* point sources) were removed and the corresponding pixels were set to the average value of the adjacent directions. In order to subtract the dust components correlated with N(H I) and $W_{\rm CO}$, the reddening map was fitted with a linear combination of the same set of N(H I) and $W_{\rm CO}$ maps for the Gould Belt and local, Perseus, and outer-arm regions described above. A detailed discussion of the results of the fit goes beyond the scope of the present work, so it is deferred to another paper (A. A. Abdo et al. 2010, in preparation), which will address the results over several interstellar complexes in the Gould Belt and will compare them with γ-ray measurements by the LAT.

The resulting $E(B-V)_{\rm res}$ residual map, obtained by subtracting from the $E(B-V)$ map the best-fit linear combination of our set of N(H I) and $W_{\rm CO}$ maps, is shown in Figure 4. The residuals typically range from −1 to +1 magnitude. Unlike in Grenier et al. (2005), both positive and negative residuals have been considered in the analysis of the γ-ray data. Residuals hint at limitations in the gas radio tracers as well as in the $E(B-V)$ map. Positive residuals can correspond to a local increase in the dust-to-gas ratio and/or to the presence of additional gas not properly accounted for in the N(H I) and $W_{\rm CO}$ maps. The latter explanation is supported by the significant correlation we will find between the $E(B-V)_{\rm res}$ map and the LAT γ-ray data (see Section 4.2.2). Figure 4 shows that at $|b| > 5^\circ$ the $E(B-V)_{\rm res}$ map is dominated by positive residuals forming structured envelopes around the CO clouds. Small negative residuals are systematically seen toward the CO cores. They may be due to a decrease in dust temperature in the denser, well shielded, parts of the molecular complexes, or to local variations of the dust-to-gas ratio. Further comparison with dust extinction tracers is needed to investigate this effect. Positive and negative residuals appear at low latitude, but, because of the pile-up of dust clouds with different temperatures along the line of sight, the temperature correction, applied by Schlegel et al. (1998) to the thermal emission to produce the $E(B-V)$ map, is not as valid near the plane as in well-resolved local clouds off the plane, in particular toward bright star-forming regions. These effects may cause the clusters of negative residuals at $|b| < 5^\circ$. We note that the positive residuals along the plane are not well correlated with the amount of self-absorbed H I found in the second quadrant (Gibson et al. 2005). The most conspicuous self-absorbed H I cloud in fact corresponds to the negative residuals seen at $130^\circ < l < 140^\circ$.

By construction, the $E(B-V)_{\rm res}$ map compensates for the limitations of the radio tracers, both by revealing non-emitting gas and by correcting the approximations applied to handle the radiative transfer of the radio lines. In particular the $E(B-V)_{\rm res}$ map depends on the optical depth correction applied to the N(H I) maps. We note that different choices of the H I spin temperature, from the optically thin case down to 250 and 125 K, change the $E(B-V)$ residuals by up to 0.2–0.3 mag on the plane and 0.1 mag at $|b| > 5^\circ$. Off the plane, the shape of the large structures of positive residuals around the Gould Belt clouds hardly changes.

The strong correlation between $E(B-V)$ residuals and γ-ray data, which will be shown in Section 4.2.2, proves that the interstellar reddening is in many directions a better tracer of the total gas column densities than the combination of H I and CO. Therefore, we will use the $E(B-V)_{\rm res}$ map to correct the standard radio and microwave tracers, very suitable for the aims of this work since, unlike reddening, they carry distance information.

3. GAMMA-RAY ANALYSIS

3.1. LAT Data

The *Fermi* LAT is a pair-tracking telescope (Atwood et al. 2009), detecting photons from ∼20 MeV to more than 300 GeV. The tracker has 18 (x, y) layers of silicon microstrip detectors interleaved with tungsten foils to promote the conversion of γ rays into electron–positron pairs (12 thin foils of 0.03 radiation lengths in the front section plus 4 thick foils of 0.18 radiation lengths in the back section; the last two layers have no conversion foils). The tracker is followed by a segmented CsI calorimeter to determine the γ-ray energy. The whole system is surrounded by a scintillator shield to discriminate the charged CR background. The instrument design and the analysis result

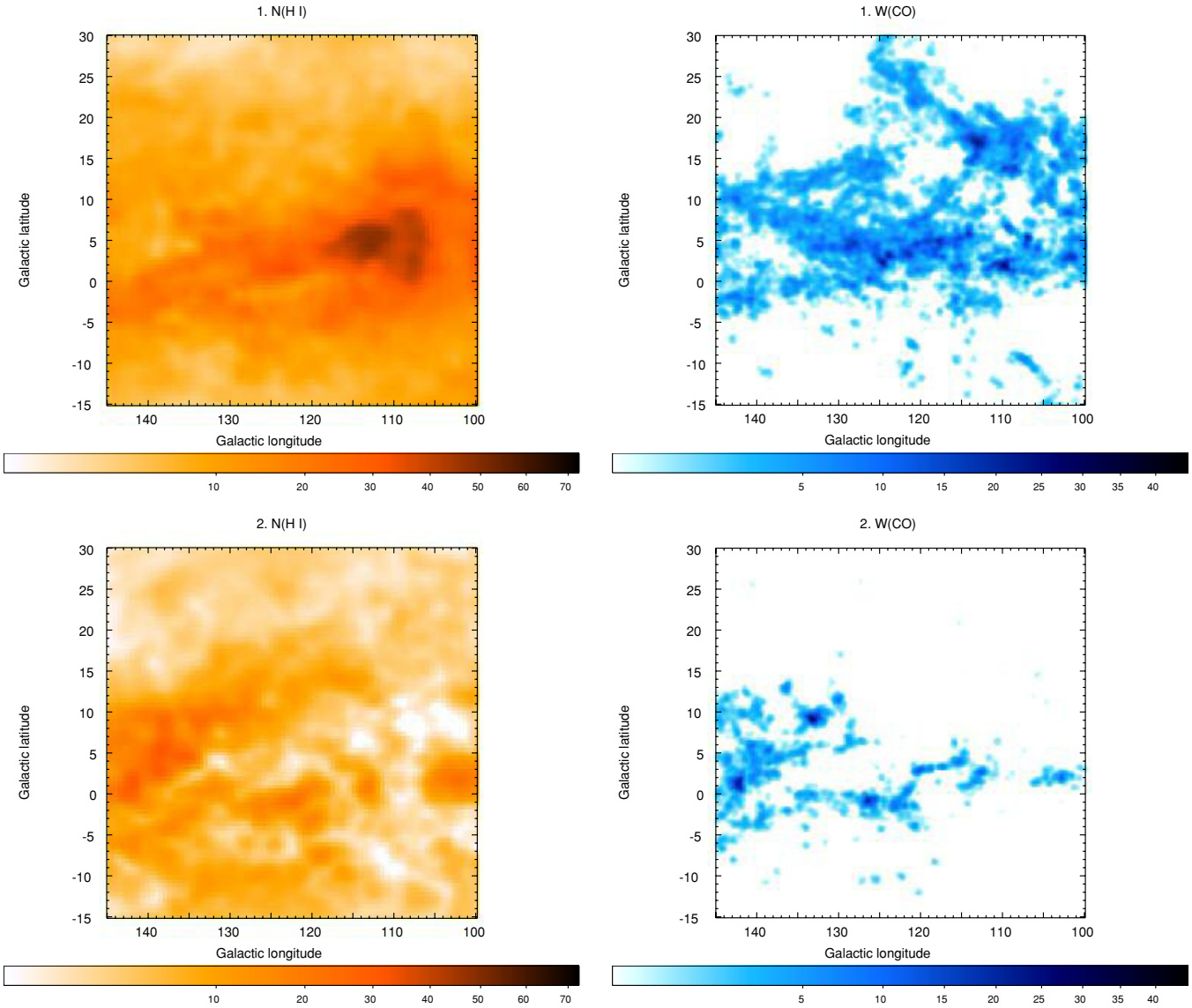

Figure 3. Maps of $N(\mathrm{H\,I})$ (units of 10^{20} atoms cm^{-2}) and W_{CO} (units of K km s^{-1}). Regions: (1) Gould Belt, (2) local arm, (3) Perseus arm, and (4) outer arm. The maps have been smoothed for display with a Gaussian with $\sigma = 1^{\circ}$. Data sources are described in the text.
(A color version of this figure is available in the online journal.)

in a peak effective area of ∼8000 cm^2 (∼6 times greater than EGRET), a field of view of ∼2.4 sr (∼5 times greater than EGRET), and a superior single photon angular resolution (for front converting photons, the 68% containment angle at 1 GeV reaches ∼0.°6 with respect to ∼1.°7 for EGRET).

Data were obtained during the period 2008 August 4–2009 July 4. The *Fermi* observatory was operated in scanning sky survey mode, rocking 35° north and south of the zenith on alternate orbits, apart from calibration runs that are excluded from the analysis. We used the data set prepared for the construction of the First Year Catalog of LAT sources (A. A. Abdo et al. 2010, in preparation), excluding brief time intervals corresponding to bright γ-ray bursts. It uses the *Diffuse* event selection, which has the least residual CR background contamination (Atwood et al. 2009). We also selected events on the basis of the measured zenith angle to limit the contamination from interactions of CRs with the upper atmosphere of the Earth. Owing to these interactions, the limb of the Earth is a very bright γ-ray source, seen at a zenith angle of ∼113° at the 565 km nearly circular orbit of *Fermi*. Since our region is close to the north celestial pole it is often observed at large rocking angles. In order to reduce the Earth albedo contamination, we accept for analysis here only events seen at a zenith angle <100°. The exposure is only marginally affected (because the detection efficiency dramatically decreases at large inclination angles), but the background rate is significantly reduced.

3.2. Model for Analysis

The analysis scheme used since the COS-B era (Lebrun et al. 1983; Strong et al. 1988; Digel et al. 1996) is based on a very simple transport model. Assuming that the ISM is transparent to γ rays, that the characteristic diffusion lengths for CR electrons and protons exceed the dimensions of cloud complexes, and that CRs penetrate clouds uniformly to their cores, the γ-ray intensity I (cm^{-2} s^{-1} sr^{-1}) in a direction (l, b) can be modeled to first order as a linear combination of contributions

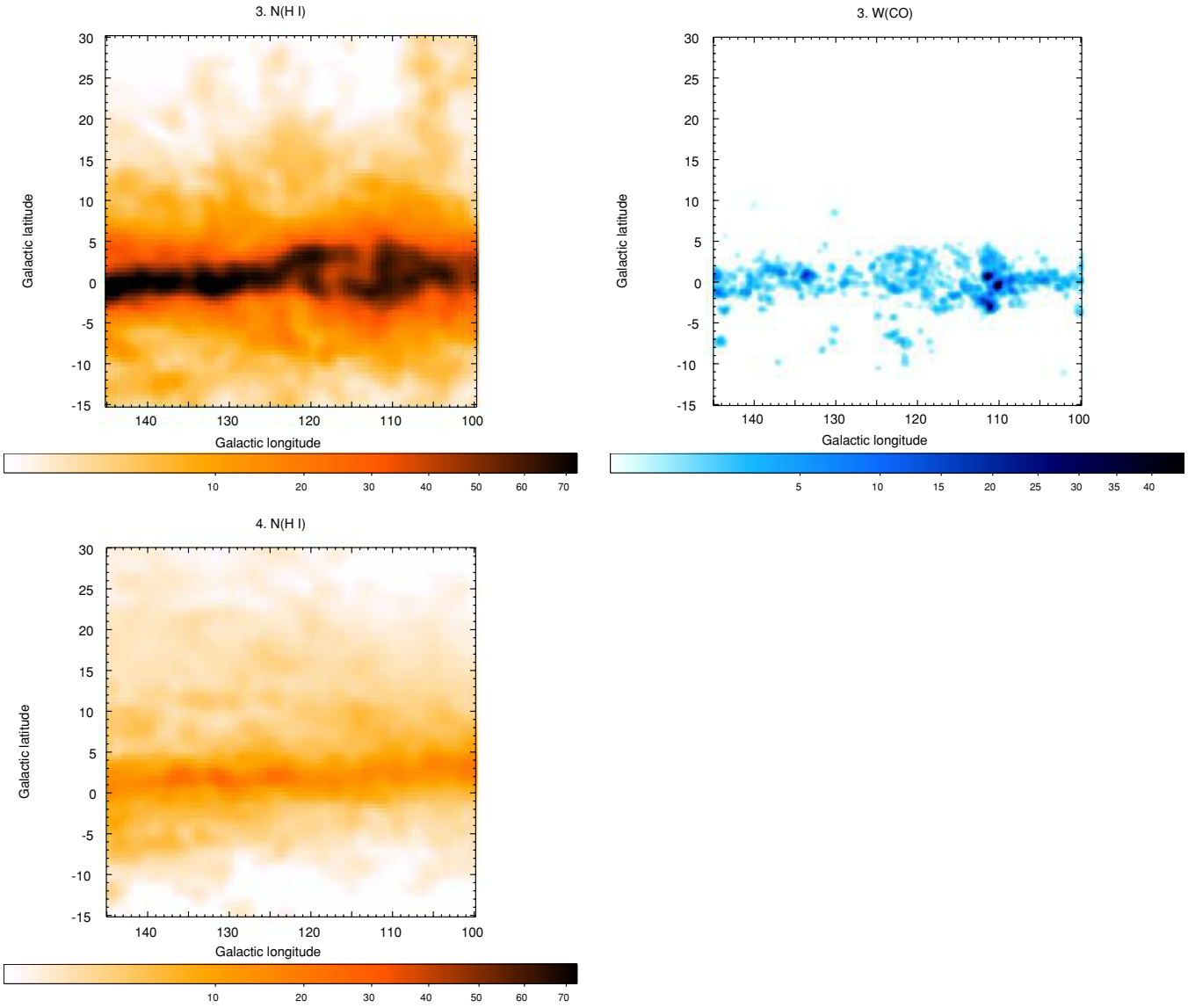

Figure 3. (Continued)

coming from CR interactions with the different gas phases in the various regions along the line of sight. We add the contribution from point-like sources and an isotropic intensity term. Several processes are expected to contribute to the latter, notably the extragalactic γ-ray background and the residual instrumental background from misclassified interactions of charged CRs in the LAT. The IC emission is also expected to be rather uniform across this small region of the sky. We used the current best models of IC emission to verify that it is statistically not distinguishable from an isotropic background over the small region of interest, at large angular distance from the inner Galaxy (see Section 3.4). The present analysis does not aim to provide meaningful results for the extragalactic background and the IC emission which will be addressed in forthcoming publications (Abdo et al. 2010, A. A. Abdo et al. 2010, in preparation).

In the absence of suitable tracers for the diffuse ionized gas (primarily H II), the derived γ-ray emissivities for neutral gas will be slightly overestimated. However, the ionized gas is contributing to $\sim$10% of the total mass and, because of its large scale height of $\sim$1 kpc above the plane (Cordes & Lazio 2002), part of its γ-ray emission will be overtaken by the isotropic term in the fit to the LAT data. So, the bias on the neutral gas emissivities should be small.

Therefore, the γ-ray intensity I, integrated in a given energy band, is modeled by Equation (1).

$$I(l,b) = \sum_{\iota=1}^{4} \left[q_{\mathrm{H\,I},\iota} \cdot N(\mathrm{H\,I})(\mathrm{l,\,b})_\iota + \mathrm{q}_{\mathrm{CO},\iota} \cdot \mathrm{W}_{\mathrm{CO}}(\mathrm{l,\,b})_\iota \right] + q_{\mathrm{EBV}} \cdot E(B-V)_{\mathrm{res}}(l,b) + I_{\mathrm{iso}} + \sum_J S_J \cdot \delta^{(2)}(l-l_J, b-b_J). \quad (1)$$

The sum over ι represents the combination of the four Galactic regions. The free parameters are the emissivities of H I gas, $q_{\mathrm{H\,I},\iota}$ (s^{-1} sr^{-1}), per unit of W_{CO} intensity, $q_{\mathrm{CO},\iota}$ (cm^{-2} s^{-1} sr^{-1} (K km s^{-1})$^{-1}$), and per unit of $E(B-V)$ residuals, q_{EBV} (cm^{-2} s^{-1} sr^{-1} mag^{-1}). I_{iso} (cm^{-2} s^{-1} sr^{-1}) is the isotropic background intensity. The contribution from point sources is

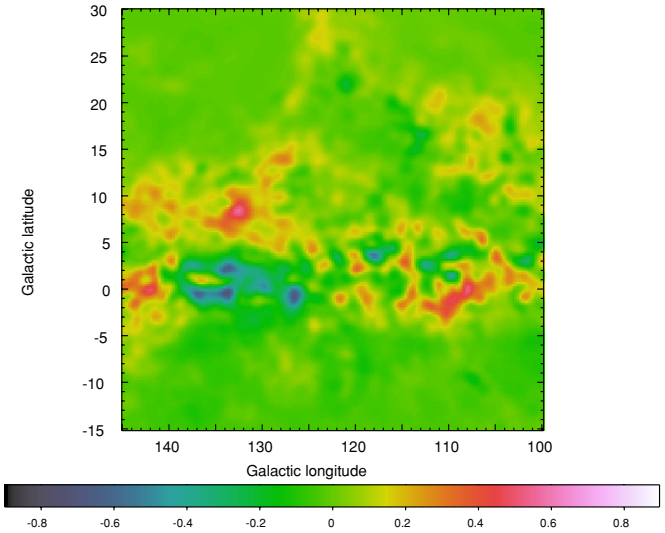

Figure 4. $E(B-V)_{\rm res}$ map: map of the reddening residuals obtained after subtraction of the parts linearly correlated with the combination of N(H I) column densities and $W_{\rm CO}$ intensities found in the four regions along the line of sight (Gould Belt, local, Perseus, and outer arms). The positive residuals surrounding CO clouds off the plane outline the potential dark-gas envelopes of the Gould Belt clouds. The map has been smoothed for display with a Gaussian with $\sigma = 1^\circ$.

(A color version of this figure is available in the online journal.)

represented by the sum over $_J$, where S_J is the integrated flux (cm^{-2} s^{-1}) of the source lying at the position (l_J, b_J).

3.3. Analysis Procedure

3.3.1. Method

We used the standard LAT analysis environment provided by the *Fermi Science Tools*.[54] The γ-ray statistics are large enough to model the spectral shape of each component as a power law in relatively narrow energy bands. This assumption, together with the iterative procedure described below in Section 3.3.2, allows the exposures and the convolution with the energy-dependent point-spread function (PSF) to be computed without forcing an a priori spectral index. The *Science Tools* provide a full convolution of the maps with the energy-dependent PSF. The *Science Tools* are also very flexible in the description of point sources (number, location, spectra). We used the `P6_V3` post launch instrument response functions (IRFs), which take into account the loss of detection efficiency due to pile-up and accidental coincidence effects in the LAT (Rando et al. 2009).

LAT data have been analyzed using a binned maximum-likelihood procedure with Poisson statistics, on a spatial grid with $0.^\circ5$ spacing in Cartesian projection. The higher energy range we have investigated starts at a few GeV, where the 68% containment angle is $\sim 0.^\circ5$ for events converting in the front section of the tracker (about a factor 2 larger for back converting events), so we cannot resolve details smaller than this in the γ-ray maps. This resolution is commensurate with that of the H I and $E(B-V)$ maps.

The analysis was performed for five contiguous energy bands: 200 MeV–400 MeV, 400 MeV–600 MeV, 600 MeV–1 GeV, 1 GeV–2 GeV, and 2 GeV–10 GeV. The energy bands were chosen wide enough to obtain stable results for the fit parameters, because large statistical fluctuations might hamper the separation of the different maps. Below 200 MeV the broad PSF does not allow an effective separation of the different maps. We are confident that between 0.2 and 10 GeV the interstellar γ-ray emission from the gas dominates over the instrumental foregrounds. The count maps in the five energy bands are shown in Figure 5.

3.3.2. Point Sources

The inclusion of sources in the analysis model is a non-trivial task because the likelihood maximization procedure (based on the optimization engine `Minuit2`[55]) is stable up to a few tens of free parameters. The sources have thus been added following an iterative procedure.

The sources were taken from the 11 month source list, which will be the basis for the First Year Catalog of LAT sources in preparation (A. A. Abdo et al. 2010, in preparation). The sources were added following the detection significance (TS) in the 11 month source list.[56] The sources were added as point-like sources keeping their positions at those given in the list while letting their power-law spectra to vary independently in each energy band. No further attempts were made in this analysis to improve the spectral modeling or to account for possible extension.

The inclusion of the sources went through the following steps, where the parameters of the diffuse emission model were always let free.

1. We started with no point sources in the model.
2. We added nine sources detected with TS $>$ 600 (hereafter bright sources). They were added to the sky model 3 at a time in order of decreasing TS, freezing at each step the previous source spectra and fitting the last three, while the diffuse parameters were always let free. Among bright sources, for the six sources lying in the region under study, we let their fluxes and spectral indexes free; for three sources lying just outside ($<5^\circ$) the region boundaries, we fixed their parameters at the values determined in the 11 month source list. These bright sources were already reported in the LAT Bright Source List (Abdo et al. 2009b): two of them are firmly identified as pulsars (0FGL J0007.4+7303 or LAT PSR J0007+7303, and 0FGL J2229.0+6114 or PSR J2229+6114), one as a γ-ray binary (0FGL J0240.3+6113 or LSI+61 303), and the others are associated with blazars.
3. We then added 52 more sources in the 11 month source list within the region boundaries with TS between 600 and $\simeq$ 25 (out of them 22 where detected with TS $>$ 100); they were added in several groups of six or five sources, with a procedure analogous to that used to handle bright sources, but only their integrated fluxes were allowed to be free, whereas the spectral indexes were fixed at the values in the source list.
4. Finally, the analysis was repeated with all the sources, letting free only the parameters of the diffuse model and of the bright sources.

The iterative procedure allows verification that only the bright sources can affect the diffuse parameters: the latter do not significantly change when less significant sources (TS $<$ 600) are added to the model. This does not apply to $I_{\rm iso}$ and $q_{\rm H\,I,\,4}$: we

[54] http://fermi.gsfc.nasa.gov/ssc/data/analysis/documentation/Cicerone/

[55] http://wwwasdoc.web.cern.ch/wwwasdoc/minuit/minmain.html

[56] The test statistic, TS, is defined as TS $= 2(\ln \mathcal{L} - \ln \mathcal{L}_0)$, where $\mathcal{L}$ and $\mathcal{L}_0$ are the maximum-likelihood values reached with and without the source, respectively.

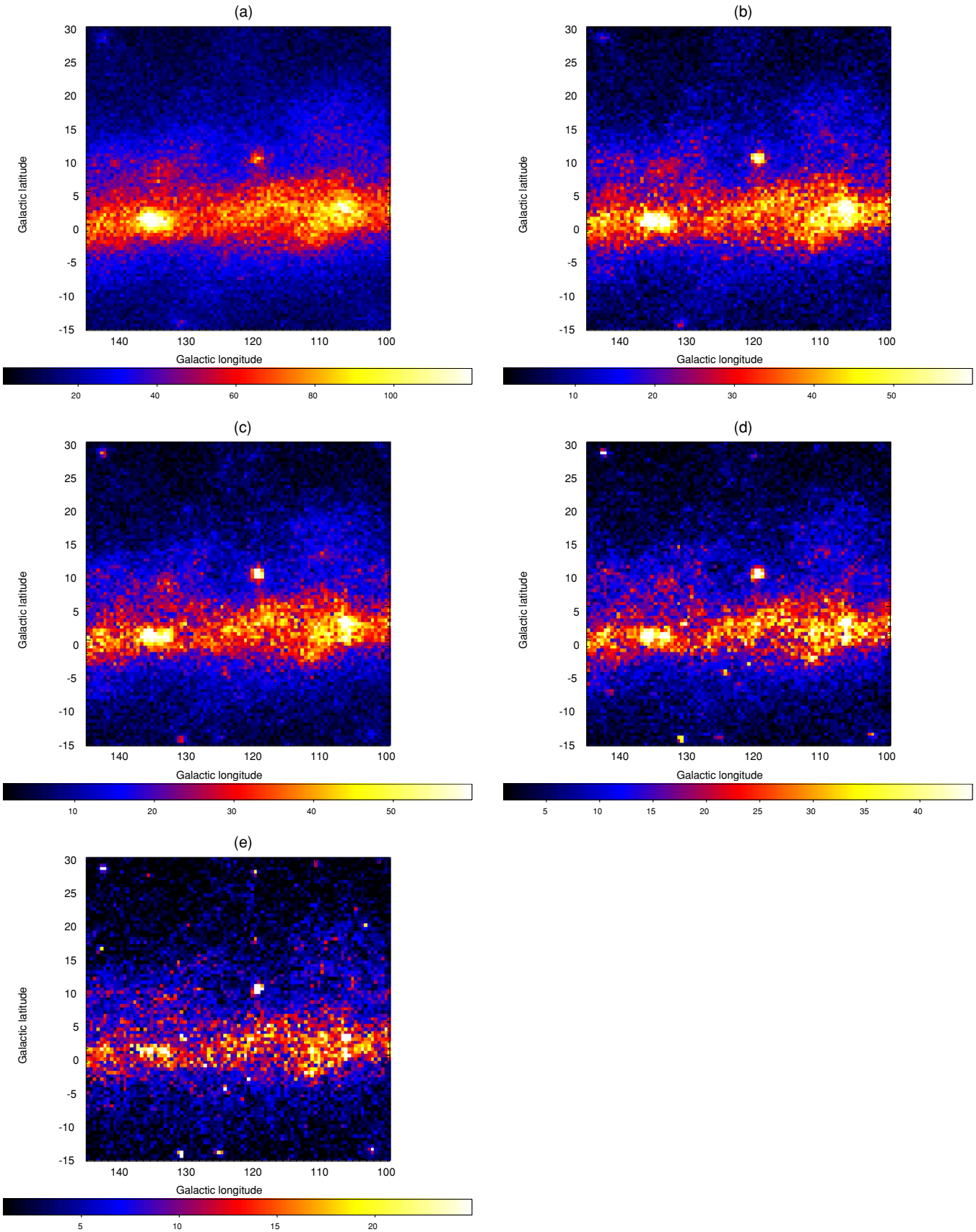

Figure 5. Gamma-ray count maps in the five energy bands: (a) 200–400 MeV, (b) 400–600 MeV, (c) 600 MeV–1 GeV, (d) 1–2 GeV, and (e) 2–10 GeV. (A color version of this figure is available in the online journal.)

note that their values keep decreasing as we add new sources down to TS $\sim$ 25. We argue that the isotropic intensity generally absorbs point sources off the plane that are not included in the analysis; as said before we are not trying to give a physical interpretation of $I_{\rm iso}$. On the other hand, given the low linear resolution in distant clouds of the outer arm and the subsequent lack of pronounced features in the map (see Figure 3), point sources at very low latitude ($|b| \lesssim 3^\circ$) can strongly bias the value of the corresponding H I emissivity, $q_{\rm H\,I,\,4}$, as separating them from the clumpy ISM emission near the plane in $0.^\circ5$ maps is difficult. Therefore, we consider this parameter only as an upper limit to the real gas emissivity in the outer arm.

3.4. Fit Results

The quality of the final fits is illustrated in the residual maps of Figure 6. The residuals, i.e., observed counts minus model-predicted counts, are expressed in standard deviation units (square root of model-predicted counts). The maps show no excesses below -4σ or above $+7\sigma$.

The best-fit parameters obtained in the five energy bands are given in Table 1, where the uncertainties correspond only to statistical errors. We have also evaluated the systematic errors due to the uncertainties on the event selection efficiency. From the comparison between Monte Carlo simulations and real observations of the Vela pulsar, they are evaluated to be 10% at 100 MeV, 5% at 500 MeV, and 20% at 10 GeV, scaling linearly with the logarithm of energy between these values. These uncertainties were parameterized into two sets of IRFs encompassing the most extreme scenarios. The last step of the analysis has been repeated using these two IRF sets and the results are assumed to bracket the systematic errors due to the event selection efficiency (shown as shaded gray areas in the following figures). Only the last step was considered, because we previously verified that only bright sources impact the parameters of the diffuse emission model.

We also verified the impact of the isotropic approximation for the IC emission, repeating the last step of the analysis including a recent model based on the GALPROP CR propagation code (see, e.g., Strong & Moskalenko 1998; Strong et al. 2004a; Porter et al. 2008). The values obtained for the parameters of the diffuse emission model were compatible with the previous results, except for the isotropic intensity.

Other systematic uncertainties will be addressed in the discussion section.

4. DISCUSSION

4.1. Emissivity Per H I Atom and Cosmic-ray Spectra

4.1.1. Consistency with Other Measurements

In Figure 7, we report the emissivity spectra per H I atom measured in the Gould Belt, the main part of the local arm and the Perseus arm. The inclusion of the $E(B-V)_{\rm res}$ map in the fit does not have a strong impact on the emissivities of the broadly distributed H I gas, which decrease by less than 10% considering the interstellar reddening in analysis.

The results we obtained in the Gould Belt and local-arm regions are consistent below 1 GeV with the measurement by Digel et al. (1996), obtained from EGRET observations of the region of Cepheus and Polaris. Above 1 GeV LAT measurements are $\sim$40% lower than those by EGRET. We will see below in Section 4.1.3 that LAT measurements are consistent with the a priori expectations for the local H I emissivity: this result confirms that, as was already deduced from LAT observations of broader regions of the sky (Abdo et al. 2009e), LAT measurements are not consistent with the GeV excess seen by EGRET, which was noticed also as an excess above 1 GeV in the emissivity of nearby H I complexes, as discussed in Digel et al. (2001).

Our spectra of the emissivity per H I atom are consistent with the results of an independent analysis carried out on LAT data to determine the local H I emissivity in a midlatitude region of the third Galactic quadrant (Abdo et al. 2009c). The latter analysis investigated a different region of the sky, but encompassing H I complexes at $\lesssim$1 kpc from the solar system, mostly located in a segment of the local arm. If we compare the present results in the main part of the local arm with those by Abdo et al. (2009c) we have excellent agreement. Therefore, we have verified that CR proton densities smoothly vary on a few kpc scale around the solar system.

4.1.2. Physical Model

We further compare our results with the predictions by GALPROP, a physical model of CR propagation in the Galaxy (see, e.g., Strong & Moskalenko 1998; Strong et al. 2004a, 2007). GALPROP solves the propagation equation for all CR species, given a CR source distribution and boundary conditions. Current GALPROP models assume a Galactocentric source distribution derived from that of pulsars (Strong et al. 2004b). The distribution used by the model adopted for this work, called `54_71Xvarh7S`, is given by Equation (2),

$$f(R) \propto \left(\frac{R}{R_\odot}\right)^{\alpha} \exp\left[-\beta\left(\frac{R-R_\odot}{R_\odot}\right)\right], \qquad (2)$$

with $\alpha = 1.25$, $\beta = 3.56$, and $R_\odot = 8.5$ kpc. A truncation is applied at $R = 15$ kpc because we do not expect many CR sources in the outermost Galaxy. This choice of parameters results in a slightly flatter radial profile of CR densities than with the pulsar distribution.

The GALPROP model `54_71Xvarh7S` is tuned to reproduce the in situ measurements of CR spectra at the solar circle. The proton spectrum is derived from a compilation of direct measurements (Alcaraz et al. 2000; Sanuki et al. 2000; Shikaze et al. 2007). The model includes the CR electron spectrum recently measured by the LAT (Abdo et al. 2009a).

Once the propagation equation is solved, GALPROP computes the emissivity for stable secondaries, in particular γ rays. The electron Bremmstrahlung component is evaluated using the formalism by Koch & Motz (1959) as explained in Strong et al. (2000). The emissivity due to p–p interactions is evaluated using the inclusive cross sections as parameterized by Kamae et al. (2006). Following the method by Dermer (1986a, 1986b), the p–p emissivity is increased to account for interactions involving CR α particles and interstellar He nuclei. This method provides an effective enhancement with respect to pure p–p emissivities, often named the nuclear enhancement factor, of $\epsilon_{\rm N} \simeq 1.45$. More recent calculations by Mori (2009), however, report values as large as $\epsilon_{\rm N} \simeq 1.75$–2 due to different CR spectral formulae (Honda et al. 2004), different ISM abundances and the inclusion of heavier nuclei both in CRs and in the ISM. Further theoretical developments are required to better constrain $\epsilon_{\rm N}$, extending the predictions from γ rays to other relevant messengers like antiprotons (Adriani et al. 2009).

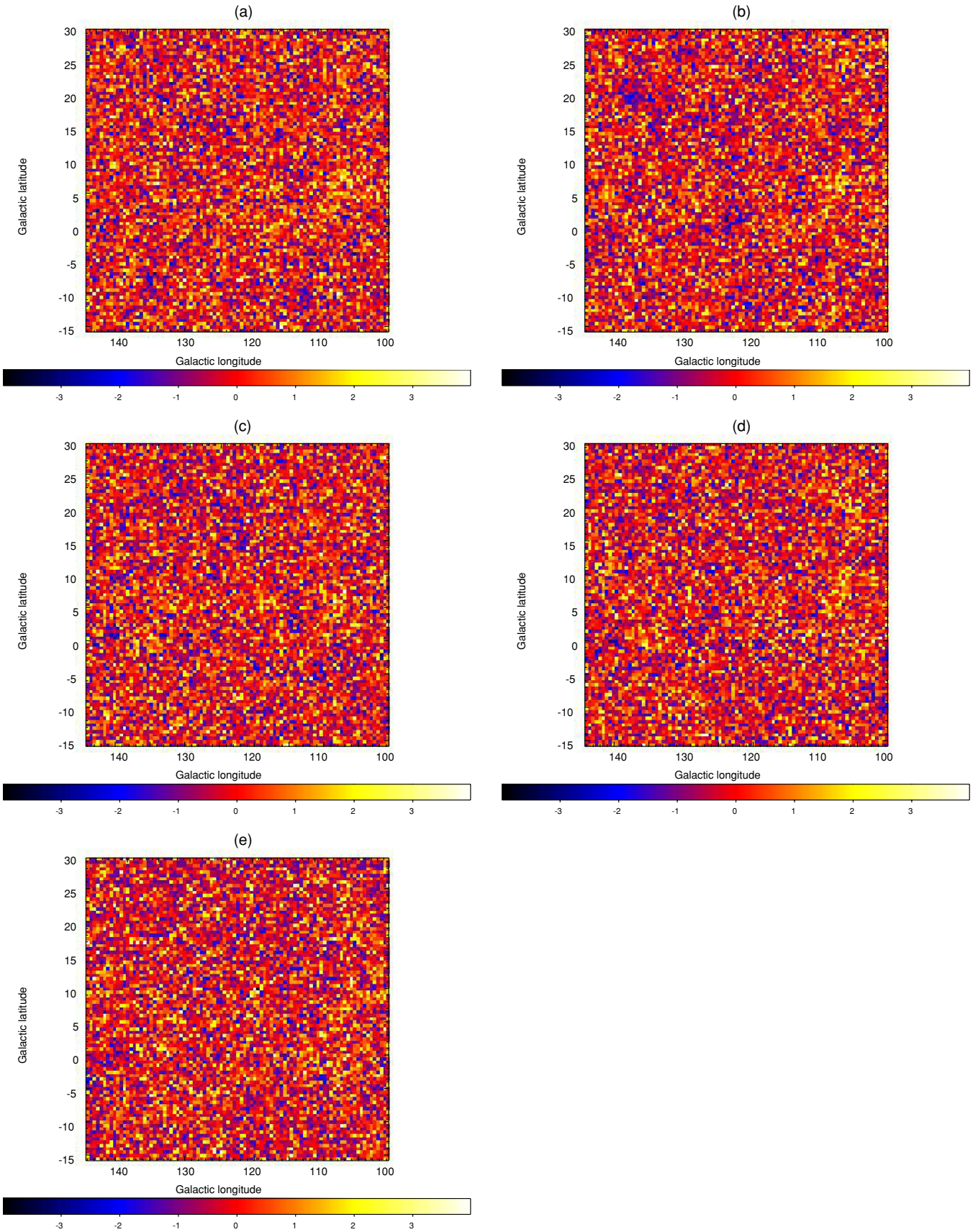

Figure 6. Gamma-ray residual maps in the same energy bands as in Figure 5. The residuals, i.e., observed counts minus model-predicted counts, are in units of the square root of the model-predicted counts (truncated between −4 and +4 for display).

(A color version of this figure is available in the online journal.)

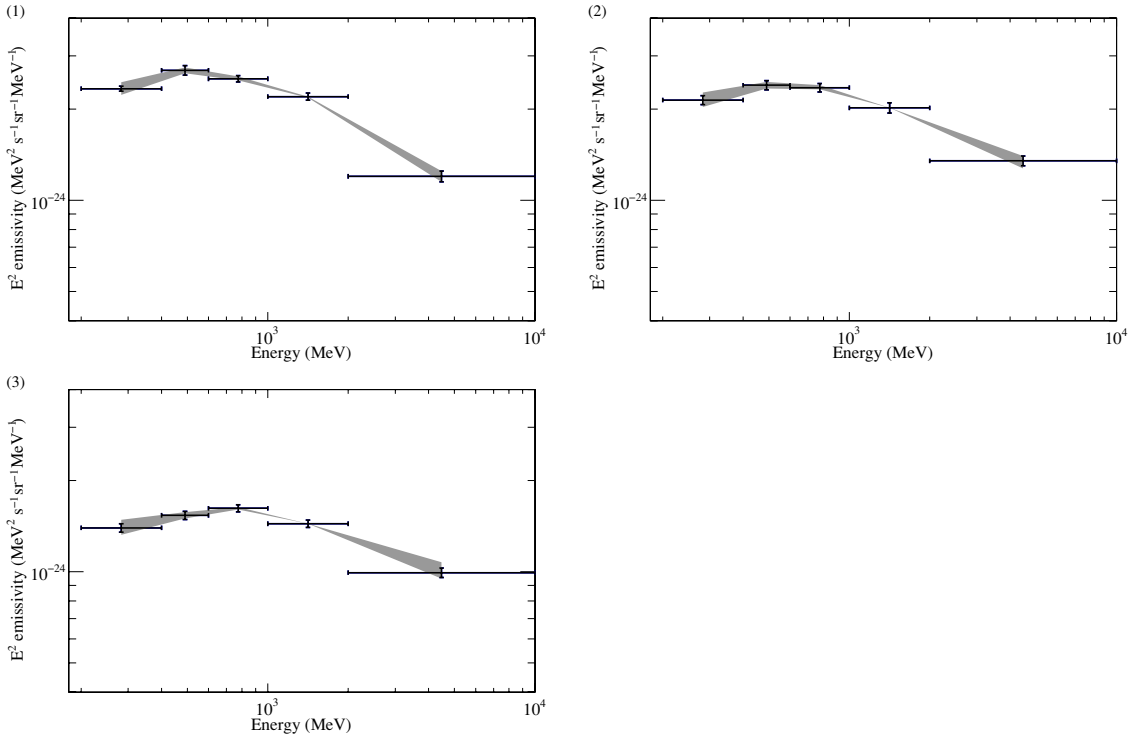

Figure 7. Emissivity spectra per H I atom as measured in the Gould Belt (1), local arm (2), and Perseus arm (3) clouds. Horizontal bars mark the energy bands, vertical bars show the statistical uncertainties on the measurement. The shaded areas represent the systematic errors due to the uncertainties on the event selection efficiency.

Table 1
Parameters of the Diffuse Emission Model Obtained from the Fit to LAT Data

Parameter [a,b]	0.2–0.4 GeV	0.4–0.6 GeV	0.6–1 GeV	1–2 GeV	2–10 GeV
$q_{\mathrm{H\,I},1}$	0.584 ± 0.011	0.224 ± 0.008	0.168 ± 0.004	0.110 ± 0.003	0.048 ± 0.002
$q_{\mathrm{CO},1}$	1.09 ± 0.04	0.367 ± 0.017	0.318 ± 0.013	0.198 ± 0.008	0.102 ± 0.005
$q_{\mathrm{H\,I},2}$	0.536 ± 0.018	0.200 ± 0.007	0.157 ± 0.005	101 ± 0.004	0.054 ± 0.002
$q_{\mathrm{CO},2}$	1.67 ± 0.17	0.47 ± 0.06	0.44 ± 0.04	0.26 ± 0.03	0.087 ± 0.014
$q_{\mathrm{H\,I},3}$	0.349 ± 0.011	0.128 ± 0.004	0.108 ± 0.003	0.072 ± 0.002	0.0397 ± 0.0014
$q_{\mathrm{CO},3}$	1.17 ± 0.15	0.52 ± 0.06	0.37 ± 0.04	0.24 ± 0.03	0.115 ± 0.016
$q_{\mathrm{H\,I},4}$	0.33 ± 0.04	0.101 ± 0.017	0.114 ± 0.013	0.103 ± 0.009	0.032 ± 0.005
q_{EBV}	16.7 ± 1.0	6.0 ± 0.4	3.49 ± 0.27	2.28 ± 0.18	0.80 ± 0.11
I_{iso}	4.67 ± 0.10	1.19 ± 0.04	0.92 ± 0.03	0.63 ± 0.02	0.371 ± 0.0017

Notes.
[a] Units: $q_{\mathrm{H\,I},i}$ (10^{-26} s^{-1} sr^{-1}), $q_{\mathrm{CO},i}$ (10^{-6} cm^{-2} s^{-1} sr^{-1} (K km s^{-1})$^{-1}$), q_{EBV} (10^{-6} cm^{-2} s^{-1} sr^{-1} mag^{-1}), I_{iso} (10^{-6} cm^{-2} s^{-1} sr^{-1}).
[b] The subscripts refer to the different regions under analysis: (1) Gould Belt, (2) local arm, (3) Perseus arm, and (4) outer arm and beyond.

4.1.3. Emissivity in the Gould Belt

In Figure 8, we compare the emissivity spectrum per H I atom we measured in the Gould Belt with the GALPROP predictions. We find the latter to be ≃50% lower at all energies. As we have just discussed, a large part of this excess (∼30%) can be explained by the uncertainties in the contribution from interactions involving CR and ISM nuclei other than protons. The remaining ∼20% excess can be explained by systematic uncertainties in the CR proton spectra at the Earth (∼20%), the N(H I) column-density derivation, and the kinematical separation of emission from the outer Galaxy.

The H I emissivity in the Gould Belt clouds (within 300 pc from the solar system) is thus consistent with the hypothesis that the gas is interacting with CRs with the same spectra measured at Earth. Figure 8 shows the GALPROP model scaled by +50% to highlight that the spectral shape is in good agreement with our results.

The H I spin temperature of 125 K (chosen to have a straightforward comparison with earlier analyses) is among the lowest values reported in the literature. A higher temperature would imply a higher emissivity, therefore a larger discrepancy with the GALPROP model (e.g., $q_{\mathrm{H\,I},1}$ increases by another 5%–10% if we take $T_S = 250$ K as recently suggested by Dickey et al. 2009).

4.1.4. H I Emissivity Gradient

It is evident from Figure 7 that the H I emissivity decreases from the Gould Belt to the Perseus arm, as expected from the declining distribution of candidate CR sources in the outer Galaxy. Figure 9 shows the emissivity ratios between the more distant regions and the Gould Belt. Systematic errors due to the event selection efficiency are not relevant for these ratios, because the emissivity spectra are similar.

The emissivity spectrum in the local arm is 10% lower than in the Gould Belt. The GALPROP model predicts such a decrease because of the change in Galactocentric radius from the solar circle to the main part of local arm, located in this direction at ∼9.5 kpc.

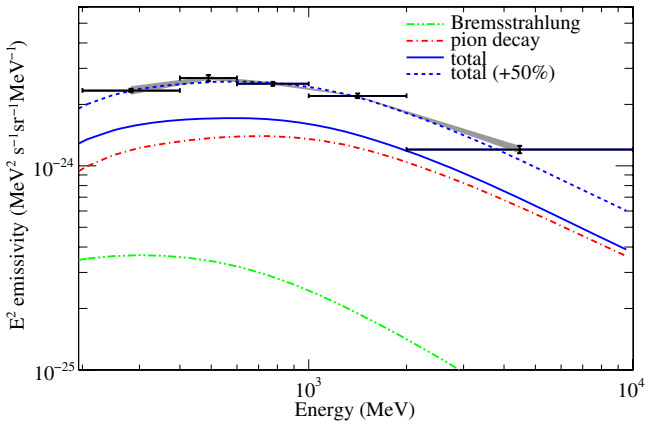

Figure 8. H I emissivity spectrum in the Gould Belt, as shown in Figure 7. The curves represent the predictions by GALPROP `54_71Xvarh7S`. The total emissivity from the model has been increased by 50% to reproduce our measurements.

(A color version of this figure is available in the online journal.)

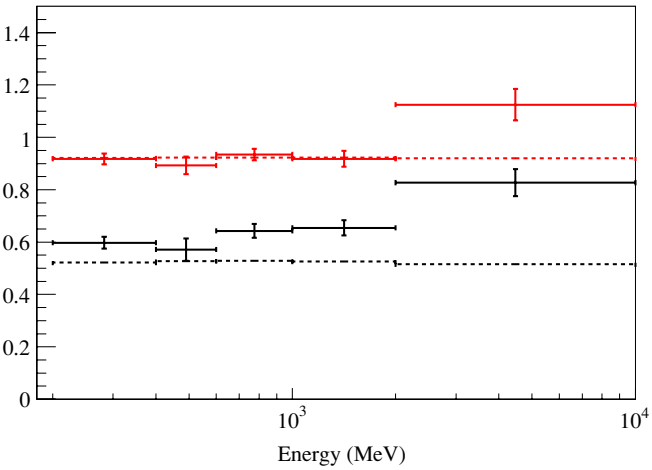

Figure 9. Emissivities measured in the Perseus arm—black—and in the local arm—light (red)—relative to those in the Gould Belt. Horizontal bars mark the energy ranges, vertical bars show statistical uncertainties. The dashed lines represent the GALPROP predictions.

(A color version of this figure is available in the online journal.)

A further decline in $q_{\rm H\,I}$ is expected between the local and Perseus arms, but Figure 9 shows that the measured $q_{\rm H\,I}$ gradient is significantly shallower than the GALPROP prediction. In Figure 10, we compare the H I emissivity integrated above 200 MeV predicted by GALPROP as a function of Galactocentric radius with the values we measured in the four regions defined for analysis, drawing the same conclusion. In this figure, we report the emissivity found in the outer arm, though considered only as an upper limit because its determination is probably affected by faint sources (see Section 3.3.2).

The discrepancies between the measured and predicted gradients may be due to the large uncertainty in the CR source distribution. The SNR radial distribution across the Galaxy is very poorly determined because of the small sample available and large selection effects (Case & Bhattacharya 1998). Distance and interstellar dispersion uncertainties also bias the pulsar distribution, in spite of the larger sample available (Lorimer 2004). On the other hand, the CR diffusion parameters, derived from local isotopic abundances in CRs, may not apply to the whole Galaxy, as suggested by Taillet & Maurin (2003). Self-absorption can also lead to a significant underestimate of

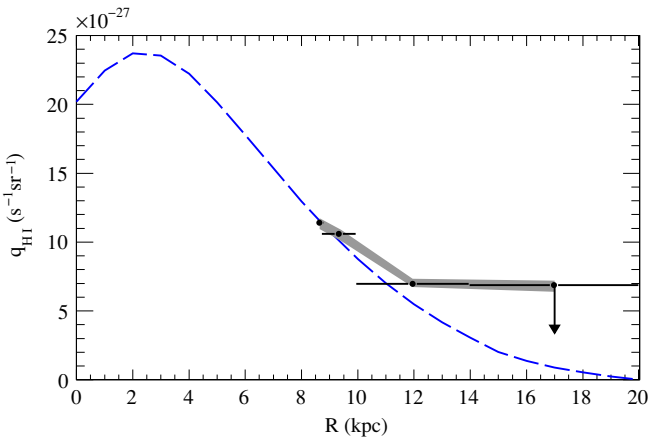

Figure 10. Radial profile with Galactocentric radius of the H I emissivity integrated between 200 MeV and 10 GeV. Black dots/horizontal bars mark the ranges in kinematic distance encompassing the Gould Belt, the main part of the local arm, the Perseus and outer arms (from left to right). Statistical uncertainties on $q_{\rm H\,I}$ are smaller than the dot dimensions. The gray shaded area shows the systematic uncertainties on the event selection efficiency. The (blue) dashed line is the GALPROP prediction scaled up by 50%.

(A color version of this figure is available in the online journal.)

N(H I) in the Perseus arm (Gibson et al. 2005), and thus to an overestimate of its γ-ray emissivity. Therefore, further investigation is needed to better understand the radial profile of the H I emissivity.

In Figure 7, the H I emissivity spectrum in the Perseus arm appears harder than expectations, thus suggesting that primary CR spectra vary across the Galaxy. We cannot, however, rule out energy-dependent systematic effects due to the separation power provided by the LAT PSF which strongly varies with energy, or a hardening due to contamination by hard unresolved point sources, like pulsars, clustering in the Perseus-arm structures.

4.2. Cloud Masses

4.2.1. CO

Because the γ-ray emission from molecular clouds is primarily due to H_2 and the molecular binding energy is negligible with respect to the energy scale of the γ radiation processes, the emissivity per H_2 molecule is twice the emissivity per H I atom. Under the hypothesis that the same CR flux penetrates the H I and CO phases of a cloud, we can assume that $q_{{\rm CO},\,i} = 2\,X_{{\rm CO},\,i} \cdot q_{{\rm H\,I},\,i}$ in each region to derive the CO-to-H_2 conversion factor, $X_{\rm CO}$.

We have performed a maximum-likelihood linear fit $q_{{\rm CO},\,i} = X_{{\rm CO},\,i} \cdot 2q_{{\rm H\,I},\,i} + \overline{q}_i$ between the $q_{{\rm CO},\,i}$ and $q_{{\rm H\,I},\,i}$ values found in the various energy bands for each region. We have taken into account the errors and covariances obtained from the γ-ray fits for both $q_{\rm H\,I}$ and $q_{\rm CO}$. Systematic errors due to the event selection efficiency do not affect the derivation of the $X_{\rm CO}$ slope because the H I and CO emissivities have similar spectra. The results are shown in Figure 11, and the best-fit parameters are reported in Table 2. We observe a good linear correlation between $q_{\rm H\,I}$ and $q_{\rm CO}$ that lends support to the assumption that CRs penetrate molecular clouds uniformly to their cores (still under debate; see, e.g., Gabici et al. 2007).

Figure 12 shows the $X_{\rm CO}$ variation with Galactocentric radius. Our measurements are consistent with previous γ-ray estimates in this region of the sky (Digel et al. 1996), but they are more precise, especially in the outer Galaxy. For the segment of the Perseus arm near NGC 7538, we have lowered the statistical uncertainty from ∼40% to 10%. The results suggest

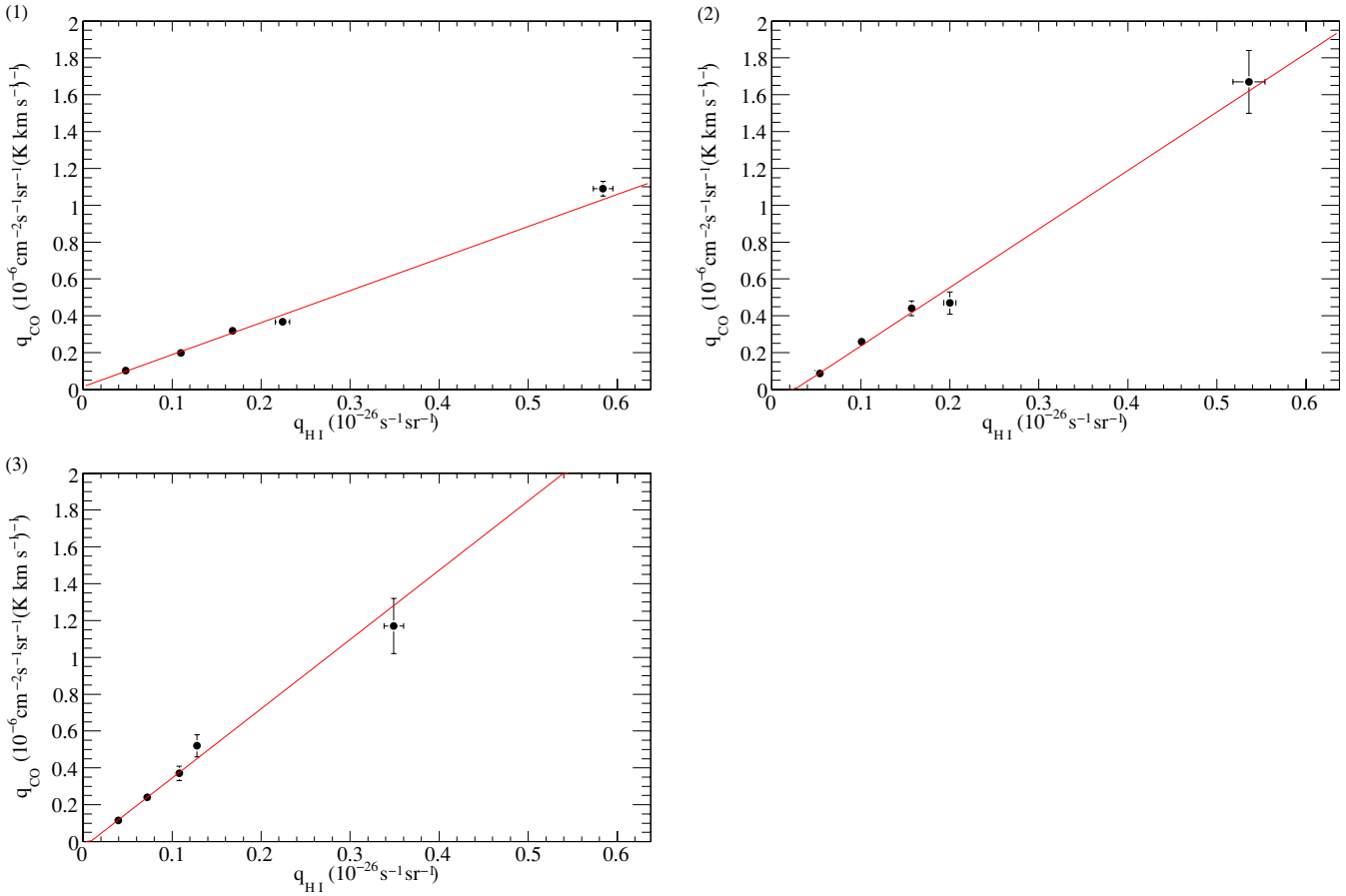

Figure 11. Correlation between the H I and CO emissivities obtained in the five energy bands for each region under analysis: (1) Gould Belt, (2) local arm, and (3) Perseus arm. Error bars show the statistical uncertainties on $q_{\mathrm{H\,I},\,i}$ and $q_{\mathrm{CO},\,i}$. The (red) lines give the best linear fits.
(A color version of this figure is available in the online journal.)

Table 2
Results of the Linear Fits between the H I and CO Emissivities in the Different Regions (1: Gould Belt, 2: local arm, 3: Perseus arm):
$q_{\mathrm{CO},\,i} = X_{\mathrm{CO}\,i} \cdot 2q_{\mathrm{H\,I},\,i} + \bar{q}_i$

Region	X_{CO}[a]	$\bar{q}$[b]
1	0.87 ± 0.05	0.015 ± 0.012
2	1.59 ± 0.17	−0.08 ± 0.03
3	1.9 ± 0.2	−0.03 ± 0.03

Notes.
[a] Units: 10^{20} cm^{-2} (K km s^{-1})$^{-1}$).
[b] Units: 10^{-6} cm^{-2} s^{-1} sr^{-1} (K km s^{-1})$^{-1}$.

an increase of X_{CO} in the outer Galaxy, as expected from the metallicity gradient (see, e.g., Rolleston et al. 2000). The X_{CO} measurements in external galaxies indeed show a metallicity dependence possibly caused by CO photodissociation and poor self-shielding in low-metallicity environments (Israel 1997, 2000).

Contamination from unresolved point sources with a spatial distribution closely related to that of the clouds is expected in star-forming regions which can produce young pulsars, SNRs, and massive binaries. This effect is unlikely in the Gould Belt clouds (Cassiopeia, Cepheus, and Polaris), first because they form few high-mass stars, second because of the good linear resolution of the γ-ray maps of these nearby clouds. Their proximity ($\lesssim$300 pc) and the $\sim$0.°5 angular resolution of the LAT in the higher energy band imply a linear resolution $\lesssim$3 pc, which allows an efficient separation between diffuse emission and point sources. The contamination by point sources is limited for similar reasons in the nearby local arm, $\lesssim$1 kpc away, but it cannot be clearly ruled out in the Perseus-arm clouds which are known to form massive star clusters (see, e.g., Sandell & Sievers 2004).

We cannot exclude separation problems between the γ-ray emission from the CO cores and their surrounding H I envelopes. The separation, based on the spatial distribution of the different phases, becomes less efficient with increasing distance due to the lower linear resolution. Moreover, we have verified that the presence of γ rays associated with the dark-gas envelopes around the CO cores affects the determination of the CO-to-H_2 factor in more distant, not so well-resolved, clouds (whereas the impact is negligible in the closer clouds). Excluding the $E(B-V)_{\mathrm{res}}$ map from the model yields a $\sim$30% increase of X_{CO} in the Perseus arm. Unfortunately, the $E(B-V)_{\mathrm{res}}$ map is not reliable near the plane because of the confusion along the line of sight that prevents an adequate temperature correction and the removal of clusters of IR point sources, so this difference has to be considered as a systematic error on X_{CO} in the Perseus arm.

Whether the present X_{CO} gradient can be fully attributed to the metallicity gradient, or partially to unresolved sources, H I and CO separation problems, or gas not traced by H I and CO, needs further investigation, primarily at higher resolution when more high-energy LAT data become available to profit from the better angular resolution. For the moment, the fact that the present X_{CO} determination does not depend on energy (see Figure 11)

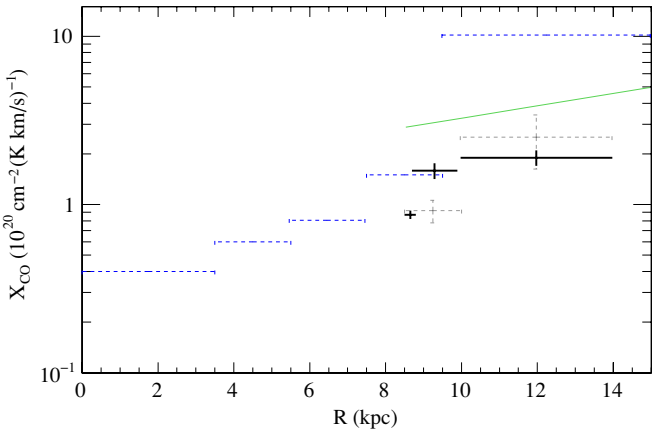

Figure 12. X_{CO} as a function of Galactocentric radius. The solid-line (black) points represent our measurements: horizontal bars mark the ranges of kinematic distance encompassing the Gould Belt and the local and Perseus arms (from left to right), vertical bars show the statistical uncertainties on X_{CO} (errors are statistical only; possible systematics are discussed in the text in Section 4.2.1). Dashed (blue) lines represent the values used in GALPROP by Strong et al. (2004b). The solid (green) line shows the X_{CO} function determined by Nakanishi & Sofue (2006) from CO data and virial masses (adapted to the rotation curve assumed for our analysis). The dashed (gray) points show the previous EGRET measurements in the region of Cepheus and Polaris (Digel et al. 1996).

(A color version of this figure is available in the online journal.)

suggests that unresolved sources and separation of the different gas phases do not significantly influence the result. The results shown in Figure 12 indicate significantly smaller X_{CO} values in the outer Galaxy than those used by Strong et al. (2004b) in GALPROP and systematically smaller values than the $X_{CO}(R)$ relation determined by Arimoto et al. (1996) and Nakanishi & Sofue (2006) using CO data and virial masses.

The X_{CO} values shown in Table 2 have been used to estimate cloud masses using Equation (3),

$$M = 2\ \mu\ m_{\rm H}\ d^2\ X_{\rm CO} \int W_{\rm CO}(l, b)\, d\Omega, \qquad (3)$$

where d is the distance of the cloud, $m_{\rm H}$ is the H atom mass, and $\mu = 1.36$ is the mean atomic weight per H atom in the ISM. We did not use the kinematic distances inferred from CO surveys, but we adopted more precise estimates available in the literature. The results are given in Table 3. The errors include only the statistical uncertainties on X_{CO}.

To investigate the discrepancies found between the different determinations of X_{CO}, we calculated the virial masses for well-resolved clouds off the plane. The virial masses have been obtained from the CO velocity dispersion for a spherical mass distribution with density profile $\propto 1/r$, following Equation (4),

$$M = \frac{3}{2}\,\frac{r}{G}\,\sigma_v^2, \qquad (4)$$

where r is the cloud radius, σ_v is the velocity dispersion, and G is Newton's constant. The velocity dispersion has been measured for each line of sight and the average value in the sample has been taken as the characteristic σ_v in the cloud. This method limits the impact of the obvious velocity gradients in these clouds. Because the virial mass heavily depends on the estimate of the characteristic radius and on the cutoff applied in its evaluation, we considered both the effective radius $r_A = \sqrt{A/\pi}$ (where A is the geometrical area of the cloud) and the intensity-weighted radius $\langle r \rangle = \left(\sum_\iota W_{{\rm CO}\,\iota}\ r_\iota\right) / \left(\sum_\iota W_{{\rm CO}\,\iota}\right)$ (where r_ι is the distance of pixel ι to the peak W_{CO} pixel). We truncated the calculation at 1% of the W_{CO} peak in both cases. We find that the virial masses are systematically larger than the X_{CO} derived masses by a factor 1.5–3. This discrepancy in the nearby clouds is comparable to that shown in Figure 12 between the γ-ray estimates of X_{CO} and the $X_{CO}(R)$ function by Nakanishi & Sofue (2006) which relies on virial masses. The γ-ray estimates are independent from the chemical, dynamical, and thermodynamical state of the clouds, but they can suffer from the limited resolution of γ-ray surveys and the non-uniform penetration of CRs into the dense CO cores. Conversely, the assumption of a spherical cloud in virial equilibrium against turbulent motions is rather crude. Intrinsic velocity gradients and magnetic pressure can easily bias the virial mass results.

4.2.2. Dark Gas

In order to quantify the significance of the correlation between the γ-ray intensities and the $E(B-V)_{\rm res}$ map, we have repeated the last step of Section 3.3.2 without including it in the analysis. The corresponding test statistics, TS $= 2\Delta(\ln \mathscr{L})$, obtained in the five energy bands are given in Table 4. With the addition of two free parameters ($q_{\rm EBV}$ and a spectral index), in the null hypothesis that there is no γ-ray emission associated with the $E(B-V)_{\rm res}$ map TS should follow a χ^2 distribution with two degrees of freedom. Therefore, the correlation between γ rays and $E(B-V)$ residuals is verified at a confidence level $> 99.9\%$ in all energy bands.

The magnitudes of the dust masses and dust IR emission are too low to explain this correlation by CR interactions with dust

Table 3
Masses for Specific Clouds, Complexes or Regions Obtained from CO Intensities and the X_{CO} Values in Table 2

Region	l	b	d (kpc)	$M_{\rm CO}$	$M_{\rm vir}(r_A)$	$M_{\rm vir}(\langle r \rangle)$	$M_{\rm dark}$
Cepheus	[100, 117]	[6, 22]	0.3[a]	0.37 ± 0.02	0.687	0.903	0.160 ± 0.011
Polaris	[117, 129]	[18, 30]	0.25[b]	0.052 ± 0.003	0.208	0.159	0.031 ± 0.002
Cassiopeia	[117, 145]	[2, 18]	0.3[a]	0.61 ± 0.03	0.893	1.062	0.34 ± 0.02
Gould Belt	[100, 145]	[−15, 30]	0.3	1.47 ± 0.08			
NGC 7538	[107, 115]	[−5, 5]	2.65[c]	20 ± 2			
NGC 281	[120, 125]	[−9, −5]	3.0[d]	0.79 ± 0.08	1.205	1.047	
Perseus arm	[100, 145]	[−10, 10]	3.0	57 ± 6			

Notes. For selected clouds, we also report virial masses and, in the Gould Belt, the dark-gas mass obtained from the $X_{\rm EBV}$ conversion factor determined in Section 4.2.2. All masses are in units of $10^5\ M_\odot$ and the errors include only the statistical uncertainties on X_{CO} or $X_{\rm EBV}$.

[a] Grenier et al. (1989).

[b] Heithausen & Thaddeus (1990).

[c] Moscadelli et al. (2009).

[d] Sato et al. (2007).

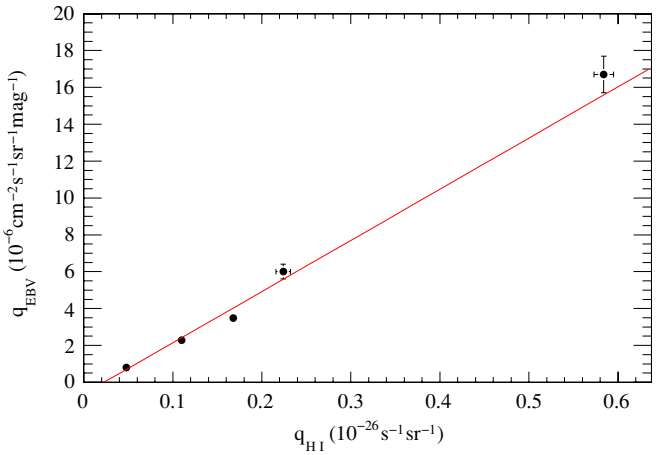

Figure 13. Correlation in the Gould Belt between the H I emissivities and the emissivities per unit of $E(B-V)_{\rm res}$. Error bars show the statistical errors obtained on both emissivities in the five energy bands. The (red) line shows the best linear fit.

(A color version of this figure is available in the online journal.)

Table 4
TS = 2Δ(ln $\mathscr{L}$) for the Inclusion of the $E(B-V)_{\rm res}$ Map in the Fit in the Different Energy Bands

Energy Range (GeV)	TS
0.2–0.4	53.8
0.4–0.6	124
0.6–1	74.6
1–2	91.8
2–10	38.2

grains or their thermal radiation. However, the correlation can be explained by CR interactions in normal gas that is not accounted for in the N(H I) and $W_{\rm CO}$ maps.

In Section 4.2.1, we have used the γ-ray emissivities per H I atom and $W_{\rm CO}$ unit to calibrate the CO-to-H_2 conversion factor, following a well-established method. We can use a similar procedure to correlate the γ-ray emissivities per H I atom and per $E(B-V)_{\rm res}$ unit in the well-resolved Gould Belt clouds (see Figure 4) where the spatial association between the H I, CO, and $E(B-V)_{\rm res}$ maps allows locating the dark gas in the absence of kinematical information.

The $q_{\rm H\,I,\,1}$ and $q_{\rm EBV}$ emissivities found in the five energy bands exhibit a tight correlation (Figure 13). As we did for CO, we fitted a linear relation, $q_{\rm EBV} = X_{\rm EBV} \cdot q_{\rm H\,I,\,1} + \overline{q}$, using a maximum-likelihood method taking into account the errors and covariances of the emissivities. The results are $X_{\rm EBV} = (28 \pm 2) \times 10^{20}$ cm^{-2} mag^{-1} and $\overline{q} = (-0.6 \pm 0.2) \times 10^{-6}$ cm^{-2} s^{-1} sr^{-1} mag^{-1}. The good linear correlation implies similar spectra for the γ-ray emission from gas seen in the H I emission line and that associated with the excess reddening, thus confirming the need for normal additional gas to explain the correlated excess of both γ rays and dust at the interface between the H I and CO emitting phases of the Gould Belt clouds.

Using the $X_{\rm EBV}$ factor in these clouds, we can calculate the additional gas mass and compare it to the molecular mass seen in CO. We restrict the comparison to the CO mass, because the more diffuse H I clouds are difficult to separate from the background H I disc extending to intermediate latitudes. To estimate the dark mass, we use only the positive residuals in the $E(B-V)_{\rm res}$ map. As discussed in Section 2.3, the small negative residuals associated with the CO cores are likely related with local variations in the dust temperature or dust-to-gas ratio. The results are given in Table 3. The errors include only the statistical uncertainties on $X_{\rm EBV}$. The additional mass in the Gould Belt clouds appears to be 40% to 60% of the CO-bright mass. We note that the sum of the dark and CO mass is closer to the virial one. We also note that FIRAS and SIMBA dust spectra in the Cepheus flare led to an independent estimate of its total mass, $M = (0.43 \pm 0.18) \times 10^5\,M_\odot$ (Bot et al. 2007), which relates well with the total (CO plus dark) mass $M = (0.53 \pm 0.02) \times 10^5\,M_\odot$ we have obtained in γ rays.

5. SUMMARY

We have analyzed the interstellar γ-ray emission observed by the *Fermi* LAT in the region of Cassiopeia and Cepheus, successfully modeling the γ-ray data as a linear combination of contributions arising from different gas complexes toward the outer Galaxy.

The separation has allowed us to verify that the γ-ray emissivity of local atomic gas is consistent with production by interactions with CRs with the same spectra as those measured near the Earth, but confirms the higher pion-decay contribution relative to some of the estimates in the literature, as found in Abdo et al. (2009c). This can be plausibly attributed to uncertainties in the local CR spectra, either in the measurement or from differences between the direct measurements and local interstellar space.

Thanks to the correlation between an excess of dust and of γ-ray emission, with a spectrum equivalent to that found for the atomic and molecular gas, we have verified the presence of an excess of gas not properly traced by the standard N(H I) and $W_{\rm CO}$ maps. In the nearby Gould Belt clouds, the dark gas forms a layer between the H I and CO phases and it represents about 50% of the mass traced in the CO-bright molecular cores.

The CR-density gradient in the outer Galaxy appears to be flatter than expectations based on the assumption that CRs are accelerated by SNRs as traced by pulsars. It is also possible that the CR spectrum in the Perseus arm is harder than in the local arm. This hardening, which needs confirmation at high resolution with more LAT data to limit the potential contamination by hard unresolved point sources, could be linked to CR diffusion not far from their sources.

We have measured $X_{\rm CO}$ in several regions from the Gould Belt to the Perseus arm. The γ-ray estimates are independent of the chemical and thermodynamical state of the gas and also from assumptions on the virial equilibrium of the clouds. They correspond to a significant but moderate increase of $X_{\rm CO}$ with Galactocentric radius outside the solar circle, from $(0.87 \pm 0.05) \times 10^{20}$ cm^{-2} (K km s^{-1})$^{-1}$ in the Gould Belt to $(1.9 \pm 0.2) \times 10^{20}$ cm^{-2} (K km s^{-1})$^{-1}$ in the Perseus arm.

The *Fermi* LAT Collaboration acknowledges generous ongoing support from a number of agencies and institutes that have supported both the development and the operation of the LAT as well as scientific data analysis. These include the National Aeronautics and Space Administration and the Department of Energy in the United States, the Commissariat à l'Energie Atomique and the Centre National de la Recherche Scientifique/Institut National de Physique Nucléaire et de Physique des Particules in France, the Agenzia Spaziale Italiana and the Istituto Nazionale di Fisica Nucleare in Italy, the Ministry of Education, Culture, Sports, Science, and Technology (MEXT), High Energy Accelerator Research Organization (KEK) and Japan Aerospace Exploration Agency (JAXA) in Japan, and the K. A. Wallenberg

Foundation, the Swedish Research Council, and the Swedish National Space Board in Sweden.

Additional support for science analysis during the operations phase is gratefully acknowledged from the Istituto Nazionale di Astrofisica in Italy and the Centre National d'Études Spatiales in France.

We thank T. H. Dame for providing moment-masked CO data including from some observations not yet published.

REFERENCES

Abdo, A. A., et al. 2009a, Phys. Rev. Lett., 102, 181101
Abdo, A. A., et al. 2009b, ApJS, 183, 46
Abdo, A. A., et al. 2009c, ApJ, 703, 1249
Abdo, A. A., et al. 2009d, ApJ, 706, L1
Abdo, A. A., et al. 2009e, Phys. Rev. Lett., 103, 251101
Abdo, A. A., et al. 2010, Phys. Rev. Lett., submitted
Acciari, V. A., et al. 2009, ApJ, 698, L133
Adriani, O., et al. 2009, Phys. Rev. Lett., 102, 051101
Aharonian, F., et al. 2008, A&A, 481, 401
Albert, J., et al. 2007, ApJ, 664, L87
Alcaraz, J., et al. 2000, Phys. Lett. B., 472, 215
Arimoto, N., Sofue, Y., & Tsujimoto, T. 1996, PASJ, 48, 275
Atwood, W. B., et al. 2009, ApJ, 697, 1071
Bloemen, H. 1989, ARA&A, 29, 469
Bot, C., et al. 2007, A&A, 471, 103
Case, G. L., & Bhattacharya, D. 1998, ApJ, 504, 761
Cordes, J. M., & Lazio, T. J. W. 2002, arXiv:astro-ph/0207156
Dame, T. M., Hartmann, D., & Thaddeus, P. 2001, ApJ, 547, 792
Dermer, C. D. 1986a, ApJ, 307, 47
Dermer, C. D. 1986b, A&A, 157, 223
Dickey, J. M., et al. 2009, ApJ, 693, 1250
Digel, S. W., Bally, J., & Thaddeus, P. 1990, ApJ, 357, L29
Digel, S. W., et al. 1996, ApJ, 463, 609
Digel, S. W., et al. 2001, ApJ, 555, 12
Gabici, S., Aharonian, F. A., & Blasi, P. 2007, Ap&SS, 309, 365
Gibson, S. J., et al. 2005, ApJ, 626, 195
Grenier, I. A., Casandjian, J. M., & Terrier, R. 2005, Science, 307, 1292
Grenier, I. A., et al. 1989, ApJ, 347, 231
Heithausen, A., & Thaddeus, P. 1990, ApJ, 353, L49
Honda, M., et al. 2004, Phys. Rev. D, 70, 043008
Israel, F. P. 1997, A&A, 328, 471
Israel, F. P. 2000, in Molecular Hydrogen in Space, ed. F. Combes & G. Pineau des Forêts (Cambridge: Cambridge Univ. Press), 293
Kalberla, P. M. W., et al. 2005, A&A, 440, 775
Kamae, T., et al. 2006, ApJ, 647, 692
Koch, H. W., & Motz, J. W. 1959, Rev. Mod. Phys., 31, 920
Lebrun, F., et al. 1983, ApJ, 274, 231
Lorimer, D. R. 2004, in IAU Symp. 218, Young Neutron Stars and Their Environments, ed. F. Camilo & B. M. Gaensler (Dordrecht: Kluwer), 105
Mohan, R., Dwarakanath, K. S., & Srinivasan, G. 2004a, JA&A, 25, 143
Mohan, R., Dwarakanath, K. S., & Srinivasan, G. 2004b, JA&A, 25, 185
Moscadelli, L., et al. 2009, ApJ, 693, 406
Mori, M. 2009, Astropart. Phys., 31, 341
Nakanishi, H., & Sofue, Y. 2006, PASJ, 58, 847
Perrot, C. A., & Grenier, I. A. 2003, A&A, 404, 519
Porter, T. A., et al. 2008, ApJ, 682, 400
Rando, R., et al. 2009, arXiv:0907.0294
Rolleston, W. R. J., et al. 2000, A&A, 363, 537
Sandell, G., & Sievers, A. 2004, ApJ, 600, 269
Sanuki, T., et al. 2000, ApJ, 545, 1135
Sato, M., et al. 2007, PASJ, 59, 743S
Shikaze, Y., et al. 2007, Astropart. Phys., 28, 154
Schlegel, D. J., Finkbeiner, D. P., & Davis, M. 1998, ApJ, 500, 525
Sodroski, T. J., et al. 1995, ApJ, 452, 262
Sodroski, T. J., et al. 1997, ApJ, 480, 173
Solomon, P. M., & Barret, J. W. 1991, in IAU Symp. 218, Dynamics of Galaxies and Their Molecular Cloud Distribution, ed. F. Combes & F. Casoli (Dordrecht: Kluwer), 235
Strong, A. W., & Moskalenko, I. V. 1998, ApJ, 509, 212
Strong, A. W., Moskalenko, I. V., & Ptuskin, V. S. 2007, Annu. Rev. Nucl. Part. Syst., 57, 285
Strong, A. W., Moskalenko, I. V., & Reimer, O. 2000, ApJ, 537, 763
Strong, A. W., Moskalenko, I. V., & Reimer, O. 2004a, ApJ, 613, 962
Strong, A. W., et al. 1988, A&A, 207, 1
Strong, A. W., et al. 2004b, A&A, 422, L47
Taillet, R., & Maurin, D. 2003, A&A, 402, 971
Ungerechts, H., Umbanhowar, P., & Thaddeus, P. 2000, ApJ, 537, 221